

# Probing the puncture for black hole simulations

J. David Brown

Department of Physics, North Carolina State University, Raleigh, NC 27695 USA

With the puncture method for black hole simulations, the second infinity of a wormhole geometry is compactified to a single “puncture point” on the computational grid. The region surrounding the puncture quickly evolves to a trumpet geometry. The computational grid covers only a portion of the trumpet throat. It ends at a boundary whose location depends on resolution. This raises the possibility that perturbations in the trumpet geometry could propagate down the trumpet throat, reflect from the puncture boundary, and return to the black hole exterior with a resolution-dependent time delay. Such pathological behavior is not observed. This is explained by the observation that some perturbative modes propagate in the conformal geometry, others propagate in the physical geometry. The puncture boundary exists only in the physical geometry. The modes that propagate in the physical geometry are always directed away from the computational domain at the puncture boundary. The finite difference stencils ensure that these modes are advected through the boundary with no coupling to the modes that propagate in the conformal geometry. These results are supported by numerical experiments with a code that evolves spherically symmetric gravitational fields with standard Cartesian finite difference stencils. The code uses the Baumgarte–Shapiro–Shibata–Nakamura formulation of Einstein’s equations with 1+log slicing and gamma–driver shift conditions.

## I. INTRODUCTION

The puncture method [1, 2] for black hole simulations works remarkably well. Initially, each black hole is represented as a wormhole. The second infinity of each wormhole is compactified to a point on the computational grid called a puncture. The spatial geometry is evolved using finite differencing with the Baumgarte–Shapiro–Shibata–Nakamura (BSSN) formulation of Einstein’s evolution equations [3, 4] and the standard gauge conditions consisting of 1+log slicing [5] and gamma–driver shift [6].

computational grid. The puncture itself is not a point in the computational grid, since the gravitational field diverges there. (Alternatively, one can apply a regularization scheme to keep the fields finite at the puncture [11, 12, 13].)

The spatial metric for the initial wormhole slice is written as  $ds^2 = \psi^4(dr^2 + r^2d\Omega^2)$ , where  $d\Omega^2$  is the metric on the unit sphere. The conformal factor  $\psi$  diverges like  $\psi \sim 1/r$  at the puncture. With 1+log slicing and an initially constant lapse, the initial wormhole slice evolves to a slice that is left–right symmetric in the Penrose diagram. The gamma–driver shift condition, which is built from the conformal metric, breaks the left–right symmetry. This allows the gamma–driver shift to drive the grid points away from the left spatial infinity, from left to right in the Penrose diagram.

The computational grid only covers a portion of the evolved wormhole slice. That portion is indistinguishable from a portion of a “trumpet slice” of Schwarzschild. A trumpet slice is a stationary 1+log slice that asymptotically approaches the left future infinity  $i^+$ . The conformal factor for a trumpet slice diverges like  $\psi \sim 1/\sqrt{r}$ . Near the puncture  $r = 0$  the trumpet geometry consists of an infinite throat with topology  $R \times S^2$  and constant cross-sectional area.

Only a finite portion of the trumpet geometry is covered by the computational grid. The grid ends at the set of grid points that are closest to  $r = 0$ . The innermost layer of grid points can be viewed as a discrete *boundary* that divides the throat into interior and exterior regions. As discussed in Ref. [7], the innermost layer of grid points constitute a natural excision boundary. The central issue addressed in this paper is how we should view this “puncture boundary”. There is, of course, an outer boundary to the computational domain as well. The numerical relativity community has spent, and continues to spend, a good deal of effort in designing boundary conditions for

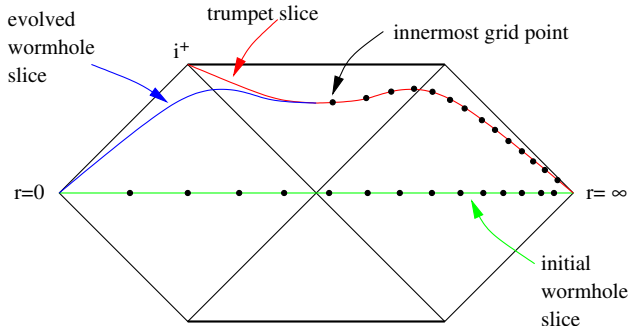


FIG. 1: Penrose diagram showing the relationship between the initial and evolved wormhole slices and a trumpet slice. The heavy dots represent the distribution of numerical grid points. This figure is a sketch based on the results from Refs. [7, 8].

The evolution of a single, spherically symmetric puncture black hole is well understood from a geometrical point of view [7, 8, 9, 10]. Figure 1 shows the Penrose diagram for a Schwarzschild black hole. The initial wormhole slice stretches between the two spacelike infinities. The puncture at  $r = 0$  coincides with the left spacelike infinity. Heavy dots mark the locations of points in the

the outer boundary. (See, for example, Ref. [14].) Should we also worry about boundary conditions at the puncture boundary?

One might argue that the puncture boundary cannot affect the exterior evolution of the black hole since it lies entirely in the black hole interior. The situation is not that simple. We know from the analysis of hyperbolicity for BSSN with standard gauge conditions that there are a number of modes that travel with superluminal speeds [15, 16]. These modes represent the gauge freedom in the system, the freedom to change the slicing and spatial coordinates. In particular, these modes do not violate the constraints [13]. Nevertheless, it is possible that a gauge wave could travel into the black hole, reflect from the artificial puncture boundary, and propagate back to the black hole exterior. This raises a number of questions. What are the boundary conditions at the puncture boundary? Are they determined by the finite difference stencil? How do the boundary conditions affect the reflected waves?

A more alarming issue is how the grid resolution might affect waves that reflect from the puncture boundary. As the computational grid is refined, grid points are added closer to the puncture point  $r = 0$ . The innermost layer of grid points is moved farther into the trumpet throat, so the distance is increased between the puncture boundary and any finite location, say, the black hole horizon. Of course, when we refine the grid the coordinate location of the puncture boundary changes by an infinitesimal amount proportional to the grid spacing. However, the proper distance from the horizon to the puncture boundary changes by a finite amount because the geometry diverges at  $r = 0$ . This raises the possibility that wave reflections from the puncture boundary will be delayed as the grid resolution is increased.

In Sec. II I present simulations of a scalar field on a cylinder  $R \times S^2$  with puncture compactification. Spherically symmetric wave pulses are sent down the cylinder and allowed to reflect from the puncture boundary. This system exhibits the pathological behavior described above. Specifically, the reflected waves show a clear resolution-dependent time delay. Moreover, we find that the form of the reflected wave is affected by the choice of finite difference stencil at the puncture boundary.

It appears that such pathological behavior does *not* occur in black hole simulations that use the puncture method. This paper is devoted to explaining why this is so. The picture that emerges can be summarized as follows. The initial wormhole data evolves very rapidly into a trumpet configuration. For the trumpet geometry, only two of the characteristic fields are outgoing at the puncture boundary.<sup>1</sup> These modes have sufficiently

large positive speeds to allow perturbations to propagate from the puncture boundary to the black hole exterior. In effect, these modes propagate in the *conformal geometry*, not the physical geometry. As such, they do not sense the movement of the puncture boundary when the grid resolution is changed. The remaining characteristic fields have negative coordinate speeds at the puncture boundary. If a perturbation occurs in one of these modes, the time it takes to reach the boundary will depend on resolution. This raises the possibility that one of these incoming modes will be coupled to an outgoing superluminal mode at the puncture boundary and give rise to a resolution-dependent reflection. Numerical simulations indicate that there are no such couplings. This can be understood by considering the finite differencing scheme as it appears in both the physical and conformal geometries. For the outgoing superluminal modes, the finite difference stencil is equivalent to a typical stencil that would be used to evolve smooth fields at the origin of a smooth geometry with topology  $R^3$ . For the modes that propagate in the physical geometry, with topology  $R \times S^2$ , the stencil is one sided at the puncture boundary. These ingoing modes are simply advected off the grid with no coupling to the outgoing modes or to each other.

Section III begins with a review of the covariant formulation of BSSN with standard gauge conditions [17]. I then present a detailed derivation of the characteristic fields and speeds for this system. The analysis uses the “frozen coefficients” approximation, defined by a small amplitude, high frequency limit for perturbations on a background solution. In this way the characteristic fields (or “modes”) are identified as perturbations that can be realized numerically. I also define a “gauge system” that has the same superluminal characteristics as the full system of BSSN with 1+log slicing and gamma-driver shift. The gauge system is linear. Useful insights into the full system can be gained by examining the simple gauge system.

In Sec. IV I show graphs of the characteristic curves for BSSN with the standard gauge, as an initial wormhole geometry evolves to a trumpet. Here we see explicitly which modes can carry information from the puncture boundary to the black hole exterior. Some of the modes are initially outgoing at the puncture boundary, but then quickly change to incoming. In principle, these modes should be fixed by boundary conditions while they are outgoing. In practice this does not seem to be a problem, perhaps because these modes spend such a short amount of time with their characteristics outgoing at the puncture boundary.

In Sec. V I describe the results of numerical experi-

---

<sup>1</sup> Throughout this paper I use the terms “outgoing” and “outward” to mean “in the positive radial direction; away from the puncture boundary”. This differs from the common definition

---

of “outgoing” as “from the interior to the exterior of the computational domain”. Likewise, terms such as “incoming” and “inward” will mean “in the negative radial direction; toward the puncture boundary”.

ments in which the characteristic fields are evolved as perturbations on a single, stationary trumpet geometry. These experiments are used to probe the puncture boundary. The perturbations consist of a simple wave pulse of compact support in one of the incoming modes. The system is evolved and reflections in the outgoing modes are examined. This technique is used to identify any resolution-dependent time delay that might appear in the reflected waves. No such delay is found.

Section VI contains a summary and discussion of the conclusions that can be drawn from the numerical experiments.

The simulations presented in this paper use a cartoon-type code [18] based on the covariant version of BSSN described in Ref. [17]. The cartoon code is described in Appendix A. The code is designed to evolve spherically symmetric gravitational fields using standard Cartesian coordinate finite difference stencils. In Cartesian coordinates, covariant BSSN is completely equivalent to the standard BSSN system. With the covariant formulation we can define transformations between Cartesian and spherical coordinates in a meaningful way.

The cartoon code is designed to be third-order convergent. In Appendix A I present the results of a two-point convergence test with the Hamiltonian constraint and a three-point convergence test with the conformal factor. These tests confirm that the code is third-order convergent everywhere in the computational domain. It is often stated that puncture evolution codes do not converge at points near the puncture. Strictly speaking, this claim is incorrect. Although there are large finite differencing errors near the puncture, a properly constructed code will be convergent everywhere except at the puncture itself, where the conformal factor is not defined.

Appendix B contains a detailed discussion of the two techniques that I use to generate the stationary trumpet geometry for the numerical tests. I discuss how the numerical data is corrected to account for the fact that neither of these techniques yields a geometry that is precisely stationary.

## II. PUNCTURE EVOLUTION OF A SCALAR FIELD

Consider a massless scalar field  $\Phi$  propagating on a three-dimensional cylinder with topology  $R \times S^2$ . The metric is  $ds^2 = d\zeta^2 + d\theta^2 + \sin^2 \theta d\phi^2$  where  $-\infty < \zeta < \infty$  and  $\theta, \phi$  are spherical coordinates on  $S^2$ . Now compactify the second infinity  $\zeta = -\infty$  with the coordinate transformation

$$\zeta = \sqrt{1+r^2} + \log\left(\frac{r}{1+\sqrt{1+r^2}}\right). \quad (1)$$

This transformation maps the three-dimensional cylinder to  $R^3$  with a puncture at the origin  $r = 0$ . The spatial

metric  $g_{ab}$  becomes

$$ds^2 = \left(1 + \frac{1}{r^2}\right) dr^2 + d\theta^2 + \sin^2 \theta d\phi^2. \quad (2)$$

This metric agrees with the trumpet metric in the limit  $r \rightarrow 0$ . In particular, both describe a three-dimensional cylinder with constant cross-sectional area and proper length that diverges like  $1/r$ .

The scalar field equation with unit lapse and vanishing shift is

$$\partial_t \Phi = \Pi, \quad (3a)$$

$$\partial_t \Pi = g^{ab} D_a D_b \Phi. \quad (3b)$$

Here,  $D_a$  is the covariant derivative built from the metric (2).

Numerical simulations are carried out using the Cartesian coordinates defined by  $r = \sqrt{x^2 + y^2 + z^2}$ ,  $\cos \theta = z/r$ , and  $\tan \phi = y/x$ . The puncture resides at the coordinate origin. The numerical grid points lie at the intersections of the coordinate lines  $x/h = 1/2, 3/2, \dots$ ;  $y/h = 1/2, 3/2, \dots$ ; and  $z/h = 1/2, 3/2, \dots$  where  $h$  is the grid spacing. We can visualize this grid by drawing the coordinate lines  $x/h = 1/2, 3/2, \dots$  and  $y/h = 1/2, 3/2, \dots$  in the equatorial plane defined by  $z = 0$ . Figure 2 shows these coordinate lines plotted on a graph of  $\zeta$  versus  $\phi$ . The left and right edges are identified, so the figure represents an infinitely long two-dimensional cylinder with circumference  $2\pi$ . In this

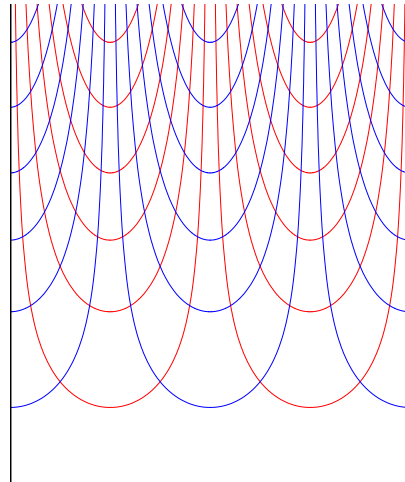


FIG. 2: Coordinates on the compactified cylinder. The left and right edges of this figure are periodically identified. The grid points lie at the intersections of the coordinate lines.

two-dimensional figure, the discrete puncture boundary consists of the four points  $(x, y) = (\pm h/2, \pm h/2)$  that coincide with the four intersections near the bottom of the figure. In the actual three-dimensional simulations, the puncture boundary consists of the eight grid points  $(x, y, z) = (\pm h/2, \pm h/2, \pm h/2)$  that are closest to the origin.

Figures 3 through 6 show a sequence of images taken from simulations at three different resolutions, low ( $h = 1/25$ ), medium ( $h = 1/50$ ), and high ( $h = 1/100$ ). The initial data consists of a spherical Gaussian pulse

$$\Phi(0) = e^{-2(r-5)^2}, \quad (4a)$$

$$\Pi(0) = -4(r-5)e^{-2(r-5)^2} \quad (4b)$$

that is traveling toward the puncture  $r = 0$ . At time  $t = 4$ , the pulse is still traveling toward the origin and the wave forms obtained from the three simulations coincide. The wave pulse hits the puncture boundary around time  $t = 8$ . The figures at times  $t = 12$  and  $t = 16$  show the reflected pulse propagating away from the origin. There is a clear dependence on resolution, with the low resolution pulse being reflected most quickly. The reflection of the medium resolution pulse is delayed relative to the low resolution case, and the reflection of the high resolution pulse is delayed even further.

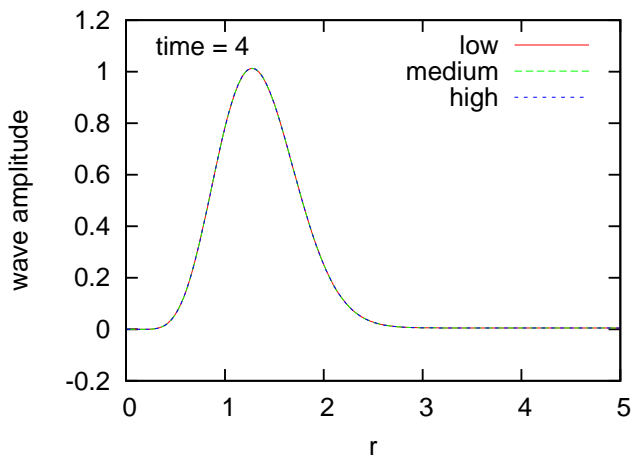


FIG. 3: Scalar field propagating on a punctured cylinder at time  $t = 4$ . Data for three resolutions are shown. The three curves overlap at this time.

The resolution dependence of the reflected pulse is precisely what we expect, based on the following analysis. Scalar fields propagate with proper speed  $dl/dt = \pm 1$ , where  $dl$  is proper length. Then the coordinate speeds in the radial direction are  $dr/dt = \pm 1/\sqrt{g_{rr}}$ . With the metric (2), the wave speeds are  $v_{in} = -r/\sqrt{1+r^2}$  for incoming waves and  $v_{out} = r/\sqrt{1+r^2}$  for outgoing waves. The time required for a pulse to propagate from some large radius  $r_0$  to the innermost grid point at  $r \approx h/2$  and return to  $r_0$  is

$$\begin{aligned} T_h &= \int_{r_0}^{h/2} \frac{1}{v_{in}} dr + \int_{h/2}^{r_0} \frac{1}{v_{out}} dr \\ &= \text{const} - 2 \log(h). \end{aligned} \quad (5)$$

The constant in this expression is independent of grid spacing  $h$ . It follows that the time difference between

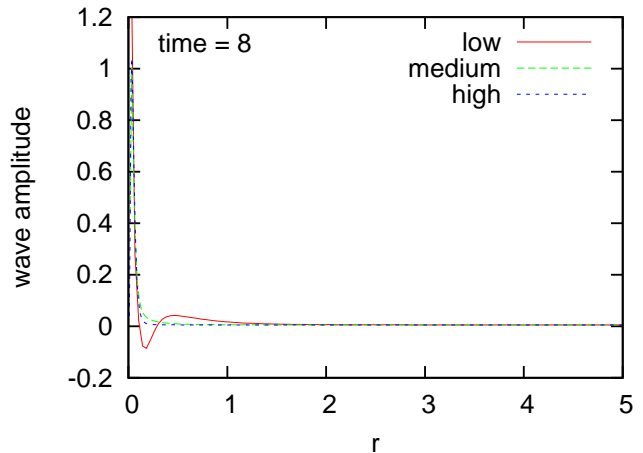


FIG. 4: Scalar field propagating on a punctured cylinder at time  $t = 8$ . The wave is interacting with the puncture boundary.

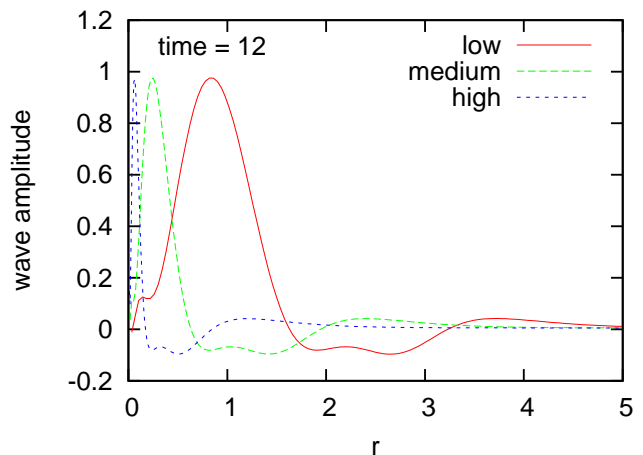


FIG. 5: Scalar field propagating on a punctured cylinder at time  $t = 12$ . The reflected waves are emerging from the puncture.

resolutions  $h$  and  $h/2$  is  $T_{h/2} - T_h = 2 \log 2 \approx 1.37$ . We can compare this with our numerical results. At time  $t = 20$ , the reflected Gaussian pulses are peaked at  $r \approx 8.35$ ,  $6.97$ , and  $5.61$  for low, medium, and high resolutions, respectively. The difference between low and medium is  $\Delta r \approx 1.38$ , whereas the difference between medium and high is  $\Delta r \approx 1.36$ . At these radial distances the wave pulses travel with coordinate speeds very close to unity. Thus, the spatial separations of  $1.38$  and  $1.36$  are remarkably close to what we would expect given a time lag of  $1.37$ .

It is important to keep in mind that the reflection is artificial. The compactification has introduced an inner, “puncture boundary.” For the ideal problem of a scalar field propagating on an infinite cylinder, the wave pulse would continue to travel down the cylinder with no re-

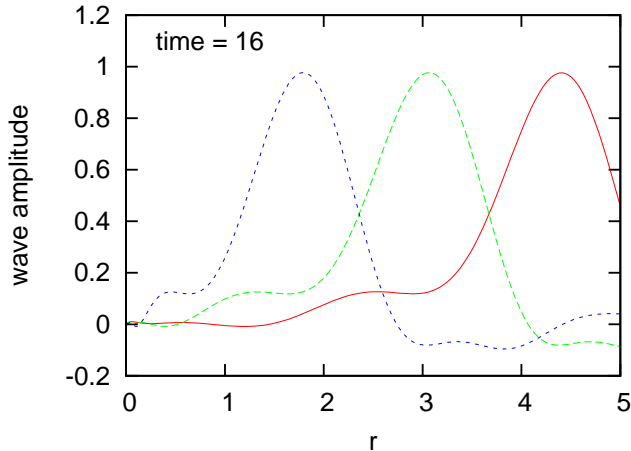


FIG. 6: Scalar field propagating on a punctured cylinder at time  $t = 16$ . The reflected pulse shows a distinct time lag that increases with resolution.

flection. We can approach this ideal behavior by increasing the resolution. When we increase the resolution the puncture boundary is pushed farther down the cylinder and the artificial reflection is postponed. In principle, the artificial reflection can be postponed indefinitely. Unfortunately, this is not feasible in practice. For example, if we want the reflected pulse to be delayed by a time of, say, 20, then Eq. (5) shows that the required resolution is  $h \approx e^{-10} \approx 1/22000$ .

Now consider how the finite difference stencil affects the reflected pulse. The simulations presented above use standard centered fourth-order stencils. For example, for the first and second derivatives of  $\Phi$  with respect to the coordinate  $z$ , we have

$$(\partial_z \Phi)_k = \frac{1}{12h} (\Phi_{k-2} - 8\Phi_{k-1} + 8\Phi_{k+1} - \Phi_{k+2}), \quad (6a)$$

$$(\partial_z^2 \Phi)_k = \frac{1}{12h^2} (-\Phi_{k-2} + 16\Phi_{k-1} - 30\Phi_k + 16\Phi_{k+1} - \Phi_{k+2}), \quad (6b)$$

where  $k$  labels grid points. These finite difference derivatives are fourth-order accurate. Alternatively, we can compute the derivatives of  $\Phi$  by

$$(\partial_z \Phi)_k = \frac{1}{12h} (-3\Phi_{k-1} - 10\Phi_k + 18\Phi_{k+1} - 6\Phi_{k+2} + \Phi_{k+3}), \quad (7a)$$

$$(\partial_z^2 \Phi)_k = \frac{1}{12h^2} (11\Phi_{k-1} - 20\Phi_k + 6\Phi_{k+1} + 4\Phi_{k+2} - \Phi_{k+3}). \quad (7b)$$

This first derivative is fourth-order accurate; the second derivative is third-order accurate.

Figure 7 shows the results of a simulation in which the finite difference stencils are altered for the eight grid

points closest to the puncture. These are the eight grid points that form the discrete puncture boundary. Stencils of the form (7) were used for first and second derivatives along the  $x$ ,  $y$ , and  $z$  coordinate lines. Cross derivatives such as  $\partial_x \partial_y \Phi$  were not changed.

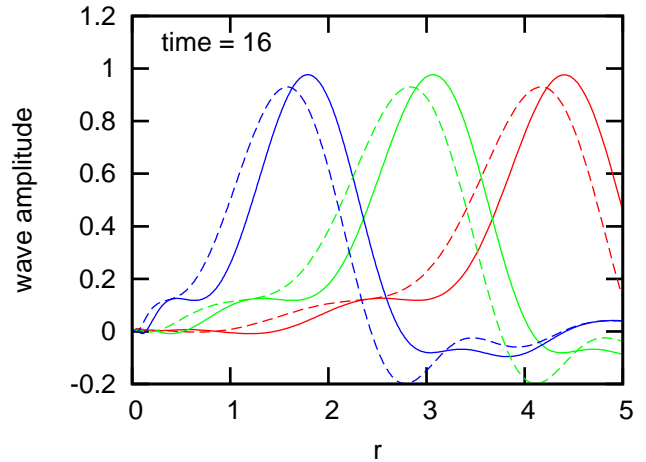


FIG. 7: Reflections from the puncture boundary of a scalar field pulse at three resolutions. The solid curves use the standard centered finite difference stencils. The dashed curves use alternative stencils for the innermost layer of grid points.

The solid curves in Fig. 7 are a repeat of the curves from Fig. 6. The dashed curves are obtained with the altered stencils applied to the innermost grid points. There is a distinct difference between these curves. With the altered stencils, the reflected pulses are shifted in time and altered in shape. This suggests that for the puncture evolution of a scalar field, the boundary conditions at the puncture boundary are determined, or at least affected, by the finite difference stencil.

### III. PERTURBATION ANALYSIS FOR BSSN AND THE STANDARD GAUGE

#### A. Covariant BSSN

The BSSN equations with 1+log slicing and gamma-driver shift conditions are written in covariant form in Ref. [17], based on earlier work in Refs. [19, 20]. The BSSN variables  $\varphi$ ,  $g_{ab}$ ,  $K$ , and  $A_{ab}$  are defined in terms of the physical metric  $g_{ab}^{\text{phys}}$  and extrinsic curvature  $K_{ab}^{\text{phys}}$  by

$$g_{ab}^{\text{phys}} = e^{4\varphi} g_{ab}, \quad (8a)$$

$$K_{ab}^{\text{phys}} = e^{4\varphi} (A_{ab} + g_{ab} K/3). \quad (8b)$$

Let  $\Delta\Gamma_{bc}^a \equiv \Gamma_{bc}^a - \hat{\Gamma}_{bc}^a$  where  $\Gamma_{bc}^a$  are the Christoffel symbols built from the conformal metric and  $\hat{\Gamma}_{bc}^a$  are the Christoffel symbols built from a background metric. Also use the notation  $\Delta\Gamma^a \equiv g^{bc} \Delta\Gamma_{bc}^a$ . The BSSN variables

include the ‘‘conformal connection vector’’ defined by

$$\Lambda^a = \Delta\Gamma^a . \quad (9)$$

In this paper I will assume that the background is flat.

The BSSN and standard gauge equations in covariant form are [17]

$$\partial_t g_{ab} = 2D_{(a}\beta_{b)} - \frac{2}{3}g_{ab}\bar{D}_c\beta^c - 2\alpha A_{ab} , \quad (10a)$$

$$\begin{aligned} \partial_t A_{ab} = & \beta^c \partial_c A_{ab} + 2A_{c(a}\partial_{b)}\beta^c - \frac{2}{3}A_{ab}\bar{D}_c\beta^c - 2\alpha A_{ac}A_b^c + \alpha A_{ab}K \\ & + e^{-4\varphi} \left[ -2\alpha D_a D_b \varphi + 4\alpha D_a \varphi D_b \varphi + 4D_{(a}\alpha D_{b)}\varphi - D_a D_b \alpha + \alpha \mathcal{R}_{ab} \right]^{\text{TF}} , \end{aligned} \quad (10b)$$

$$\partial_t \varphi = \beta^c \partial_c \varphi + \frac{1}{6}\bar{D}_c\beta^c - \frac{1}{6}\alpha K , \quad (10c)$$

$$\partial_t K = \beta^c \partial_c K + \frac{\alpha}{3}K^2 + \alpha A_{ab}A^{ab} - e^{-4\varphi} (D^2\alpha + 2D^a\alpha D_a\varphi) , \quad (10d)$$

$$\begin{aligned} \partial_t \Lambda^a = & \beta^c \dot{D}_c \Lambda^a - \Delta\Gamma^c \dot{D}_c \beta^a + g^{bc} \dot{D}_b \dot{D}_c \beta^a + \frac{2}{3}\Delta\Gamma^a \bar{D}_c \beta^c + \frac{1}{3}D^a \bar{D}_c \beta^c \\ & - 2A^{bc} (\delta_b^a \partial_c \alpha - 6\alpha \delta_b^a \partial_c \varphi - \alpha \Delta\Gamma_{bc}^a) - \frac{4}{3}\alpha g^{ab} \partial_b K , \end{aligned} \quad (10e)$$

$$\partial_t \alpha = \beta^c \dot{D}_c \alpha - 2\alpha K , \quad (10f)$$

$$\partial_t \beta^a = \beta^c \dot{D}_c \beta^a + \frac{3}{4}B^a , \quad (10g)$$

$$\partial_t B^a = \beta^c \dot{D}_c B^a + (\partial_t \Lambda^a)_{\text{rhs}} - \beta^c \dot{D}_c \Lambda^a - \eta B^a , \quad (10h)$$

where

$$\mathcal{R}_{ab} \equiv -\frac{1}{2}g^{cd} \dot{D}_c \dot{D}_d g_{ab} + g_{c(a} \dot{D}_{b)} \Lambda^c + g^{de} \Delta\Gamma_{de}^c \Delta\Gamma_{(ab)c} + g^{cd} \left( 2\Delta\Gamma_{c(a}^e \Delta\Gamma_{b)ed} + \Delta\Gamma_{ac}^e \Delta\Gamma_{ebd} \right) . \quad (11)$$

In the equations above it is assumed that  $A \equiv g^{ab}A_{ab} = 0$  is enforced. The superscript TF denotes the trace-free part of the expression in square brackets, defined with respect to either the conformal metric or the physical metric. The term  $(\partial_t \Lambda^a)_{\text{rhs}}$  in Eq. (10h) must be replaced by the right-hand side of Eq. (10e). The operator  $D_a$  denotes the covariant derivative with respect to the conformal metric  $g_{ab}$ . The operator  $\bar{D}_a$  denotes the covariant derivative with respect to the initial conformal metric,  $g_{ab}(0)$ . The operator  $\dot{D}_a$  denotes the covariant derivative with respect to the (flat) background metric.

If the initial conformal metric is flat and the coordinates are Cartesian, then the equations of motion (10a–e) above are identical to the original BSSN equations [3, 4]. Likewise, Eq. (10f) is the usual 1+log slicing condition and Eqs. (10g,h) are the gamma-driver shift conditions. Note that the gamma-driver shift equations include all advection terms. With this choice, Eqs. (10g,h) are equivalent to the single equation spatial gauge condition used by the Goddard group [21]. In the final section I discuss how the results are changed if one or more of the advection terms are dropped.

For the BSSN formulation of Einstein’s equations the constraints are defined by

$$\mathcal{H} = \frac{2}{3}K^2 - A_{ab}A^{ab} + e^{-4\varphi} (R - 8D^a\varphi D_a\varphi - 8D^2\varphi) , \quad (12a)$$

$$\mathcal{M}_a = g^{bc} \dot{D}_b A_{ac} - A_{ab} \Delta\Gamma^b - A_c^b \Delta\Gamma_{ab}^c + 6A_a^c \partial_c \varphi - \frac{2}{3}\partial_a K , \quad (12b)$$

$$\mathcal{C}^a = \Lambda^a - \Delta\Gamma^a , \quad (12c)$$

where  $R$  is the conformal Ricci scalar. Here,  $\mathcal{H} = 0$  and  $\mathcal{M}_a = 0$  are the usual Hamiltonian and momentum constraints. The constraint  $\mathcal{C} = 0$  arises from the definition of the conformal connection vector.

## B. Characteristic fields

Hyperbolicity for systems of partial differential equations with first order time and second order space deriva-

tives can be analyzed using the pseudodifferential operator method of Refs. [22, 23]. This technique was first ap-

plied to BSSN with standard gauge conditions by Beyer and Sarbach [15].

It will be useful to begin by adopting a condensed notation. The BSSN plus standard gauge equations (10) have the quasilinear form

$$\partial_t q = A^a(q)\partial_a q + B(q)v + C(q), \quad (13a)$$

$$\partial_t v = D^{ab}(q)\partial_a\partial_b q + E^a(q)\partial_a v + F(q, \partial q, v) \quad (13b)$$

where  $q$  represents the ‘‘coordinate variables’’  $g_{ab}$ ,  $\varphi$ ,  $\alpha$ , and  $\beta^a$  and  $v$  represents the ‘‘velocity variables’’  $A_{ab}$ ,  $K$ ,  $\Lambda^a$ , and  $B^a$ . The coefficients  $A^a$ ,  $B$ ,  $C$ ,  $D^{ab}$ , and  $E^a$  depend on the  $q$ 's. The function  $F$  is a quadratic polynomial in the variables  $\partial_a q$ ,  $v$  with coefficients that depend on the  $q$ 's.

Let  $\hat{q}$ ,  $\hat{v}$  denote a solution of Eqs. (13) and consider perturbations  $\tilde{q}$ ,  $\tilde{v}$  about this solution:

$$q = \hat{q} + \tilde{q}, \quad (14a)$$

$$v = \hat{v} + \tilde{v}. \quad (14b)$$

The ‘‘frozen coefficients’’ approximation is defined by a small amplitude, high frequency limit as follows. The coefficients in Eqs. (13) and their spatial derivatives are assumed to be of order unity or smaller. The perturbation fields have small amplitudes proportional to  $\epsilon$  and large wave numbers proportional to  $k$ . To be precise, we let  $\partial\tilde{q} \sim \tilde{v} \sim \mathcal{O}(\epsilon)$  where  $\partial$  denotes a space or time derivative. For higher order derivatives,  $\partial\partial\tilde{q} \sim \partial\tilde{v} \sim \mathcal{O}(\epsilon \cdot k)$ . The coordinate perturbation  $\tilde{q}$  satisfies  $\tilde{q} \sim \mathcal{O}(\epsilon/k)$ . In the limit as  $\epsilon \rightarrow 0$  and  $k \rightarrow \infty$ , the leading order (nonvanishing) terms in Eqs. (13) are

$$\partial_t \tilde{q} = A^a(\hat{q})\partial_a \tilde{q} + B(\hat{q})\tilde{v}, \quad (15a)$$

$$\partial_t \tilde{v} = D^{ab}(\hat{q})\partial_a\partial_b \tilde{q} + E^a(\hat{q})\partial_a \tilde{v}. \quad (15b)$$

Equation (15a) is derived from the  $\mathcal{O}(\epsilon)$  terms in Eq. (13a), and Eq. (15b) is derived from the  $\mathcal{O}(\epsilon \cdot k)$  terms in Eq. (13b). Equations (15) define the principal part of the system (13). Note that the coefficients  $A^a$ ,

$B$ ,  $D^{ab}$ , and  $E^a$  are functions of the unperturbed coordinates  $\hat{q}$ . Below, I will drop the hats from the unperturbed fields for notational simplicity.

The hyperbolicity of the system is analyzed by setting the perturbation to a single Fourier mode with wave number  $k_a$ :

$$\tilde{q}(t, x) = \frac{\check{q}}{i|k|} e^{i\omega t + ik_a x^a}, \quad (16a)$$

$$\tilde{v}(t, x) = \check{v} e^{i\omega t + ik_a x^a}. \quad (16b)$$

Here,  $|k| \equiv \sqrt{k_a g^{ab} k_b}$  and  $g_{ab}$  is the unperturbed conformal metric. The unit normal to the wave front is denoted  $n_a \equiv k_a/|k|$ . The indices on  $k_a$  and  $n_a$  are raised and lowered by the unperturbed conformal metric. Note that Eq. (16a) implies  $n^a \partial_a \tilde{q} = \check{q} e^{i\omega t + ik_a x^a}$ .

Now let  $\mu \equiv \omega/|k|$ . The linear Eqs. (15) for the perturbations become a set of linear algebraic equations for the Fourier coefficients:

$$\mu \check{q} = A^a n_a \check{q} + B \check{v}, \quad (17a)$$

$$\mu \check{v} = D^{ab} n_a n_b \check{q} + E^a n_a \check{v}. \quad (17b)$$

The principal symbol  $\mathcal{P}$  is the matrix defined by the right-hand side of these equations,

$$\mathcal{P} = \begin{pmatrix} A^a n_a & B \\ D^{ab} n_a n_b & E^a n_a \end{pmatrix}. \quad (18)$$

The system of differential equations (13) is strongly hyperbolic if  $\mathcal{P}$  possesses a complete set of eigenvectors with real eigenvalues.

The characteristic fields for the system are obtained from the left eigenvectors of the principal symbol. Let  $(\xi, \zeta)$  denote such an eigenvector; that is,  $(\xi, \zeta)\mathcal{P} = \mu(\xi, \zeta)$ . The characteristic field associated with this eigenvector is  $\chi = \xi n^a \partial_a \tilde{q} + \zeta \tilde{v}$ . It satisfies  $\partial_t \chi = \mu n^a \partial_a \chi$  in the frozen coefficients approximation.

---

We now spell out the results explicitly for the BSSN plus standard gauge equations. The principal parts of these

equations are

$$\partial_t \tilde{g}_{ab} = \beta^c \partial_c \tilde{g}_{ab} + 2g_{c(a} \partial_{b)} \tilde{\beta}^c - \frac{2}{3} g_{ab} \partial_c \tilde{\beta}^c - 2\alpha \tilde{A}_{ab} , \quad (19a)$$

$$\partial_t \tilde{A}_{ab} = \beta^c \partial_c \tilde{A}_{ab} + e^{-4\varphi} \left[ -2\alpha \partial_a \partial_b \tilde{\varphi} - \partial_a \partial_b \tilde{\alpha} - \frac{\alpha}{2} g^{cd} \partial_c \partial_d \tilde{g}_{ab} + \alpha g_{c(a} \partial_{b)} \tilde{\Lambda}^c \right]^{\text{TF}} , \quad (19b)$$

$$\partial_t \tilde{\varphi} = \beta^c \partial_c \tilde{\varphi} + \frac{1}{6} \partial_c \tilde{\beta}^c - \frac{1}{6} \alpha \tilde{K} , \quad (19c)$$

$$\partial_t \tilde{K} = \beta^c \partial_c \tilde{K} - e^{-4\varphi} g^{ab} \partial_a \partial_b \tilde{\alpha} , \quad (19d)$$

$$\partial_t \tilde{\Lambda}^a = \beta^c \partial_c \tilde{\Lambda}^a + g^{bc} \partial_b \partial_c \tilde{\beta}^a + \frac{1}{3} g^{ab} \partial_b \partial_c \tilde{\beta}^c - \frac{4}{3} \alpha g^{ab} \partial_b \tilde{K} , \quad (19e)$$

$$\partial_t \tilde{\alpha} = \beta^c \partial_c \tilde{\alpha} - 2\alpha \tilde{K} , \quad (19f)$$

$$\partial_t \tilde{\beta}^a = \beta^c \partial_c \tilde{\beta}^a + \frac{3}{4} \tilde{B}^a , \quad (19g)$$

$$\partial_t \tilde{B}^a = \beta^c \partial_c \tilde{B}^a + g^{bc} \partial_b \partial_c \tilde{\beta}^a + \frac{1}{3} g^{ab} \partial_b \partial_c \tilde{\beta}^c - \frac{4}{3} \alpha g^{ab} \partial_b \tilde{K} . \quad (19h)$$

Recall that the hats have been dropped from the unperturbed solution. As above, we define  $|k| \equiv \sqrt{k_a g^{ab} k_b}$  and  $n_a \equiv k_a / |k|$ , so that  $n_a$  is normalized with respect to the unperturbed conformal metric:  $n_a g^{ab} n_b = 1$ . The principal symbol is defined by

$$\mu \check{g}_{ab} = \beta^n \check{g}_{ab} + 2n_{(a} \check{\beta}_{b)} - \frac{2}{3} g_{ab} \check{\beta}^n - 2\alpha \check{A}_{ab} , \quad (20a)$$

$$\mu \check{A}_{ab} = \beta^n \check{A}_{ab} + e^{-4\varphi} \left[ -2\alpha n_a n_b \check{\varphi} - n_a n_b \check{\alpha} - \frac{\alpha}{2} \check{g}_{ab} + \alpha n_{(a} \check{\Lambda}_{b)} \right]^{\text{TF}} , \quad (20b)$$

$$\mu \check{\varphi} = \beta^n \check{\varphi} + \frac{1}{6} \check{\beta}^n - \frac{1}{6} \alpha \check{K} , \quad (20c)$$

$$\mu \check{K} = \beta^n \check{K} - e^{-4\varphi} \check{\alpha} , \quad (20d)$$

$$\mu \check{\Lambda}^a = \beta^n \check{\Lambda}^a + \check{\beta}^a + \frac{1}{3} n^a \check{\beta}^n - \frac{4}{3} \alpha n^a \check{K} , \quad (20e)$$

$$\mu \check{\alpha} = \beta^n \check{\alpha} - 2\alpha \check{K} , \quad (20f)$$

$$\mu \check{\beta}^a = \beta^n \check{\beta}^a + \frac{3}{4} \check{B}^a , \quad (20g)$$

$$\mu \check{B}^a = \beta^n \check{B}^a + \check{\beta}^a + \frac{1}{3} n^a \check{\beta}^n - \frac{4}{3} \alpha n^a \check{K} . \quad (20h)$$

Here, the notation  $T^n \equiv T^a n_a$  is used for any tensor  $T^a$  contracted with the normal covector  $n_a$ .

Define  $e_A^a$  by  $n_a e_A^a = 0$  and  $e_A^a g_{ab} e_B^b = \delta_{AB}$ , where the upper case indices  $A, B \dots$  range over the values 1 and 2. Thus  $e_A^a$  forms an orthonormal diad in the subspace orthogonal to  $n_a$ . Indices on  $n_a$  and  $e_A^a$  are raised and lowered with the conformal metric and its inverse. For any tensor  $T_a$  we define  $T_n \equiv T_a n^a = T^a n_a \equiv T^n$  and  $T_A \equiv T_a e_A^a$ . The diad index  $A$  is raised and lowered with the identity tensor  $\delta_{AB}$  and its inverse.

With this notation we can split the principal Eqs. (20) into scalar, vector, and trace-free tensor blocks. The scalar

block is

$$\mu\check{g}_{nn} = \beta^n\check{g}_{nn} + \frac{4}{3}\check{\beta}_n - 2\alpha\check{A}_{nn} , \quad (21a)$$

$$\mu\check{g}_{AA} = \beta^n\check{g}_{AA} - \frac{4}{3}\check{\beta}_n + 2\alpha\check{A}_{nn} , \quad (21b)$$

$$\mu\check{A}_{nn} = \beta^n\check{A}_{nn} + e^{-4\varphi} \left[ -\frac{4}{3}\alpha\check{\varphi} - \frac{2}{3}\check{\alpha} - \frac{\alpha}{3}\check{g}_{nn} + \frac{2}{3}\alpha\check{\Lambda}_n + \frac{\alpha}{6}\check{g}_{AA} \right] , \quad (21c)$$

$$\mu\check{\varphi} = \beta^n\check{\varphi} + \frac{1}{6}\check{\beta}_n - \frac{1}{6}\alpha\check{K} , \quad (21d)$$

$$\mu\check{K} = \beta^n\check{K} - e^{-4\varphi}\check{\alpha} , \quad (21e)$$

$$\mu\check{\Lambda}_n = \beta^n\check{\Lambda}_n + \frac{4}{3}\check{\beta}_n - \frac{4}{3}\alpha\check{K} , \quad (21f)$$

$$\mu\check{\alpha} = \beta^n\check{\alpha} - 2\alpha\check{K} , \quad (21g)$$

$$\mu\check{\beta}_n = \beta^n\check{\beta}_n + \frac{3}{4}\check{B}_n , \quad (21h)$$

$$\mu\check{B}_n = \beta^n\check{B}_n + \frac{4}{3}\check{\beta}_n - \frac{4}{3}\alpha\check{K} , \quad (21i)$$

where  $\check{g}_{AA} \equiv \check{g}_{AB}\delta^{AB}$ . In deriving these equations I have used the fact that the perturbation  $\check{A}_{ab}$  is trace-free. This implies  $\check{A}_{nn} + \check{A}_{AA} = 0$  so that  $\check{A}_{AA}$  can be eliminated in favor of  $\check{A}_{nn}$ . The vector block of the principal symbol is

$$\mu\check{g}_{nA} = \beta^n\check{g}_{nA} + \check{\beta}_A - 2\alpha\check{A}_{nA} , \quad (22a)$$

$$\mu\check{A}_{nA} = \beta^n\check{A}_{nA} + e^{-4\varphi} \left[ -\frac{\alpha}{2}\check{g}_{nA} + \frac{\alpha}{2}\check{\Lambda}_A \right] , \quad (22b)$$

$$\mu\check{\Lambda}_A = \beta^n\check{\Lambda}_A + \check{\beta}_A , \quad (22c)$$

$$\mu\check{\beta}_A = \beta^n\check{\beta}_A + \frac{3}{4}\check{B}_A , \quad (22d)$$

$$\mu\check{B}_A = \beta^n\check{B}_A + \check{\beta}_A . \quad (22e)$$

Finally, the trace-free tensor block is

$$\mu\check{g}_{AB}^{tf} = \beta^n\check{g}_{AB}^{tf} - 2\alpha\check{A}_{AB}^{tf} , \quad (23a)$$

$$\mu\check{A}_{AB}^{tf} = \beta^n\check{A}_{AB}^{tf} - \frac{\alpha}{2}e^{-4\varphi}\check{g}_{AB}^{tf} , \quad (23b)$$

where the trace-free part of a tensor  $T_{AB}$  is defined by  $T_{AB}^{tf} \equiv T_{AB} - (T_{CD}\delta^{CD})\delta_{AB}/2$ .

The characteristic fields obtained from the scalar block are

$$\chi_1 = \check{B}^n - 8\partial_n\check{\varphi} , \quad (24a)$$

$$\chi_2 = \check{\Lambda}^n - 8\partial_n\check{\varphi} , \quad (24b)$$

$$\chi_3 = \partial_n\check{g}_{nn} + \partial_n\check{g}_{AA} , \quad (24c)$$

$$\chi_4^\pm = \frac{1}{\sqrt{2\alpha}}e^{-2\varphi}\partial_n\check{\alpha} \pm \check{K} , \quad (24d)$$

$$\chi_5^\pm = \mp\frac{3}{2}\check{A}_{nn} \pm \check{K} + e^{-2\varphi}\check{\Lambda}^n + \frac{1}{4}e^{-2\varphi}\partial_n\check{g}_{AA} - \frac{1}{2}e^{-2\varphi}\partial_n\check{g}_{nn} - 2e^{-2\varphi}\partial_n\check{\varphi} , \quad (24e)$$

$$\chi_6^\pm = \frac{3}{4}(1 - 2\alpha e^{-4\varphi})\check{B}^n \pm \alpha\check{K} + \alpha e^{-4\varphi}\partial_n\check{\alpha} \mp (1 - 2\alpha e^{-4\varphi})\partial_n\check{\beta}^n . \quad (24f)$$

These relations can be inverted for the field perturbations as long as  $(1 - 2\alpha e^{-4\varphi}) \neq 0$ . In that case we have

$$\partial_n \tilde{g}_{nn} = -\chi_1 + \frac{4}{3}\chi_2 + \frac{1}{3}\chi_3 - \frac{1}{3}(2\alpha)^{2/3}e^{-2\varphi} \frac{(\chi_4^+ + \chi_4^-)}{(1 - 2\alpha e^{-4\varphi})} - \frac{2}{3}e^{2\varphi}(\chi_5^+ + \chi_5^-) + \frac{2}{3} \frac{(\chi_6^+ + \chi_6^-)}{(1 - 2\alpha e^{-4\varphi})}, \quad (25a)$$

$$\partial_n \tilde{g}_{AA} = \chi_1 - \frac{4}{3}\chi_2 + \frac{2}{3}\chi_3 + \frac{1}{3}(2\alpha)^{2/3}e^{-2\varphi} \frac{(\chi_4^+ + \chi_4^-)}{(1 - 2\alpha e^{-4\varphi})} + \frac{2}{3}e^{2\varphi}(\chi_5^+ + \chi_5^-) - \frac{2}{3} \frac{(\chi_6^+ + \chi_6^-)}{(1 - 2\alpha e^{-4\varphi})}, \quad (25b)$$

$$\tilde{A}_{nn} = \frac{1}{3}(\chi_4^+ - \chi_4^-) + \frac{1}{3}(\chi_5^- - \chi_5^+), \quad (25c)$$

$$\partial_n \tilde{\varphi} = -\frac{1}{8}\chi_1 - \frac{1}{24}(2\alpha)^{3/2}e^{-2\varphi} \frac{(\chi_4^+ + \chi_4^-)}{(1 - 2\alpha e^{-4\varphi})} + \frac{1}{12} \frac{(\chi_6^+ + \chi_6^-)}{(1 - 2\alpha e^{-4\varphi})}, \quad (25d)$$

$$\tilde{K} = \frac{1}{2}(\chi_4^+ - \chi_4^-), \quad (25e)$$

$$\tilde{\Lambda}^n = -\chi_1 + \chi_2 - \frac{1}{3}(2\alpha)^{3/2}e^{-2\varphi} \frac{(\chi_4^+ + \chi_4^-)}{(1 - 2\alpha e^{-4\varphi})} + \frac{2}{3} \frac{(\chi_6^+ + \chi_6^-)}{(1 - 2\alpha e^{-4\varphi})}, \quad (25f)$$

$$\partial_n \tilde{\alpha} = \frac{\sqrt{2\alpha}}{2}e^{2\varphi}(\chi_4^+ + \chi_4^-), \quad (25g)$$

$$\partial_n \tilde{\beta}^n = \frac{\alpha}{2} \frac{(\chi_4^+ - \chi_4^-)}{(1 - 2\alpha e^{-4\varphi})} - \frac{1}{2} \frac{(\chi_6^+ - \chi_6^-)}{(1 - 2\alpha e^{-4\varphi})}, \quad (25h)$$

$$\tilde{B}^n = -\frac{1}{3}(2\alpha)^{3/2}e^{-2\varphi} \frac{(\chi_4^+ + \chi_4^-)}{(1 - 2\alpha e^{-4\varphi})} + \frac{2}{3} \frac{(\chi_6^+ + \chi_6^-)}{(1 - 2\alpha e^{-4\varphi})}. \quad (25i)$$

The characteristic fields from the vector and trace-free tensor blocks are

$$\chi_7 = \tilde{B}_A - \tilde{\Lambda}_A, \quad (26a)$$

$$\chi_8^\pm = \tilde{B}_A \mp \frac{2}{\sqrt{3}}\partial_n \tilde{\beta}_A, \quad (26b)$$

$$\chi_9^\pm = \tilde{\Lambda}_A - \partial_n \tilde{g}_{nA} \mp 2e^{2\varphi} \tilde{A}_{nA}, \quad (26c)$$

$$\chi_{10}^\pm = \tilde{A}_{AB}^{tf} \pm \frac{1}{2}e^{-2\varphi} \partial_n \tilde{g}_{AB}^{tf}. \quad (26d)$$

The inverse relations are

$$\partial_n \tilde{g}_{nA} = -\chi_7 + \frac{1}{2}(\chi_8^+ + \chi_8^- - \chi_9^+ - \chi_9^-), \quad (27a)$$

$$\tilde{A}_{nA} = \frac{1}{4}e^{-2\varphi}(\chi_9^- - \chi_9^+), \quad (27b)$$

$$\tilde{\Lambda}_A = -\chi_7 + \frac{1}{2}(\chi_8^+ + \chi_8^-), \quad (27c)$$

$$\partial_n \tilde{\beta}_A = \frac{\sqrt{3}}{4}(\chi_8^- - \chi_8^+), \quad (27d)$$

$$\tilde{B}_A = \frac{1}{2}(\chi_8^+ + \chi_8^-), \quad (27e)$$

$$\partial_n \tilde{g}_{AB}^{tf} = e^{2\varphi}(\chi_{10}^+ - \chi_{10}^-), \quad (27f)$$

$$\tilde{A}_{AB}^{tf} = \frac{1}{2}(\chi_{10}^+ + \chi_{10}^-). \quad (27g)$$

Note that modes  $\chi_7$ ,  $\chi_8^\pm$ , and  $\chi_9^\pm$  are vectors in the subspace orthogonal to  $n_a$ ; the index  $A$  is suppressed above. Likewise, the tensor indices  $AB$  and trace-free symbol  $tf$  have been suppressed on  $\chi_{10}^\pm$ .

The perturbations in the lapse and shift (and auxiliary field) are built from modes  $\chi_4^\pm$  and  $\chi_6^\pm$ . These can

be viewed as gauge modes. They do not violate the constraints: In the frozen coefficients approximation the perturbations of the constraints are given by

$$\begin{aligned} \tilde{\mathcal{H}} &= \frac{4}{3}e^{-4\varphi} \partial_n \chi_2 - \frac{2}{3}e^{-4\varphi} \partial_n \chi_3 \\ &\quad - \frac{2}{3}e^{-2\varphi} \partial_n (\chi_5^+ + \chi_5^-), \end{aligned} \quad (28a)$$

$$\tilde{\mathcal{M}}_n = \frac{1}{3} \partial_n (\chi_5^- - \chi_5^+), \quad (28b)$$

$$\tilde{\mathcal{M}}_A = \frac{1}{4}e^{-2\varphi} \partial_n (\chi_9^- - \chi_9^+), \quad (28c)$$

$$\tilde{\mathcal{C}}_n = -\frac{1}{3}\chi_2 + \frac{1}{6}\chi_3 + \frac{2}{3}e^{2\varphi}(\chi_5^+ + \chi_5^-), \quad (28d)$$

$$\tilde{\mathcal{C}}_A = \frac{1}{2}(\chi_9^+ + \chi_9^-). \quad (28e)$$

These perturbations depend only on modes  $\chi_2$ ,  $\chi_3$ ,  $\chi_5^\pm$ ,  $\chi_9^\pm$  and their spatial derivatives.

### C. Characteristic speeds

The phase angle for the Fourier mode (16) is  $\omega t + k_a x^a = |k|(\mu t + n_a x^a)$ . The surfaces of constant phase satisfy  $n_a dx^a/dt = -\mu$ . Let us choose the wave fronts to coincide with the surfaces  $r = \text{const}$ , where  $r$  is one of the spatial coordinates. Then the covector  $k_a$  is proportional to  $\delta_a^r$  and  $n_a = \delta_a^r/\sqrt{g^{rr}}$ . The coordinate speed of the wave is  $dr/dt$ , or

$$\text{coordinate speed} = -\mu\sqrt{g^{rr}}. \quad (29)$$

TABLE I: Coordinate and proper speeds for the scalar modes of BSSN with 1+log slicing and gamma-driver shift.

	$\chi_1$	$\chi_2$	$\chi_3$	$\chi_4^\pm$	$\chi_5^\pm$	$\chi_6^\pm$
coordinate speed	$-\beta^r$	$-\beta^r$	$-\beta^r$	$-\beta^r \pm e^{-2\varphi} \sqrt{2\alpha g^{rr}}$	$-\beta^r \pm \alpha e^{-2\varphi} \sqrt{g^{rr}}$	$-\beta^r \pm \sqrt{g^{rr}}$
near trumpet puncture	$-0.53r$	$-0.53r$	$-0.53r$	$-0.53r \pm 0.72r^{3/2}$	$-0.53r \pm 0.35r^2$	$-0.53r \pm 1$
near wormhole puncture	0	0	0	$\pm 5.7r^2$	$\pm 4.0r^2$	$\pm 1$
proper speed	0	0	0	$\pm \sqrt{2/\alpha}$	$\pm 1$	$\pm e^{2\varphi}/\alpha$
near trumpet puncture	0	0	0	$\pm 2.1/\sqrt{r}$	$\pm 1$	$\pm 2.9/r^2$
near wormhole puncture	0	0	0	$\pm 1.4$	$\pm 1$	$\pm 0.25/r^2$

This is the wave speed as seen by the ‘‘Lagrangian observers’’ who move along the  $\partial/\partial t$  coordinate lines.

For ‘‘Eulerian observers’’ who are at rest in the space-like hypersurfaces, the wave speed differs by the addition of the shift. To be precise, recall that  $-\beta^a dt$  is the change during time  $dt$  in the spatial coordinate location of an Eulerian observer. Then the coordinate distance that the wave front travels in coordinate time  $dt$ , as seen by an Eulerian observer, is the difference:  $dr - (-\beta^r dt) = dr + \beta^r dt$ .

The proper distance or time between two surfaces  $\sigma$  and  $\sigma + d\sigma$  is  $ds = d\sigma/\sqrt{\pm \partial_a \sigma \gamma^{ab} \partial_b \sigma}$ , where  $\gamma^{ab}$  are the contravariant components of a spatial or space-time metric. This result is derived by first constructing the unit normal to the  $\sigma = \text{const}$  surfaces:  $n^a = \gamma^{ab} \partial_b \sigma / \sqrt{\pm \partial_c \sigma \gamma^{cd} \partial_d \sigma}$ . The unit normal can be written as  $n^a = \partial x^a / \partial s$ , where  $s$  is proper distance or proper time. Now compute  $\partial \sigma / \partial s = \partial_a \sigma (\partial x^a / \partial s) = \sqrt{\pm \partial_a \sigma \gamma^{ab} \partial_b \sigma}$  and the desired result follows. If  $\sigma$  is one of the coordinates, the proper distance or time becomes  $ds = d\sigma / \sqrt{\pm \gamma^{\sigma\sigma}}$ .

The above argument shows that for an Eulerian observer, the wave front travels a proper distance  $(dr + \beta^r dt) / \sqrt{g_{\text{phys}}^{rr}}$  in a proper time of  $dt / \sqrt{-g_{\text{sptm}}^{tt}}$ . Here,  $g_{\text{sptm}}^{tt}$  is the contravariant  $tt$  component of the spacetime metric, related to the lapse function by  $g_{\text{sptm}}^{tt} = -1/\alpha^2$ . Putting this together we find that the proper speed of a

given mode is  $(dr/dt + \beta^r) / (\alpha \sqrt{g_{\text{phys}}^{rr}})$ , or

$$\text{proper speed} = \frac{e^{2\varphi}}{\alpha \sqrt{g^{rr}}} (\beta^r - \mu \sqrt{g^{rr}}). \quad (30)$$

Note,  $r$  can be any one of the spatial coordinates. We will often choose  $r$  to be the radial coordinate in a spherical coordinate system.

The speeds of the various modes are listed in Tables I and II. The first line in each table lists the coordinate speed of the mode in general. The second line of each table shows the coordinate speed of a radial wave near a trumpet puncture. These speeds are obtained from numerical data, which yield  $\alpha \approx 0.46r$ ,  $\beta^r \approx 0.53r$ ,  $e^{-2\varphi} \approx 0.75r$  and  $g^{rr} \approx 1$  near  $r = 0$  for a single, spherically symmetric trumpet with  $M = 1$ . (The numerical coefficients should be accurate to within 10%.) The third line of each table lists the coordinate speed of a radial wave near a wormhole puncture. These speeds are found from the initial data for a single, spherically symmetric black hole with  $M = 1$  in isotropic coordinates. They also assume the initial conditions  $\alpha = 1$  and  $\beta^a = 0$  for the lapse and shift. Then near a wormhole puncture, we have  $\alpha \approx 1$ ,  $\beta^r = 0$ ,  $g^{rr} = 1$ , and  $e^{-2\varphi} \approx 4r^2$ . The fourth line of each table lists the proper speed of each mode. The fifth and sixth lines show the proper speeds near trumpet and wormhole punctures.

The coordinate grid moves with respect to the Eulerian observers. The coordinate speed of this motion is  $\beta^r$ , and the proper speed is  $\beta^r / (\alpha \sqrt{g_{\text{phys}}^{rr}}) = e^{2\varphi} \beta^r / (\alpha \sqrt{g^{rr}})$ . Near the puncture boundary of a trumpet slice, the proper speed is  $\sim 1.5/r$ . Near a wormhole puncture boundary the proper speed is zero, assuming the shift vector vanishes.

#### D. Gauge System

Many of the issues that require close examination reside in the ‘‘gauge sector’’. We define the gauge sector by the following system of linear partial differential equa-

tions:

$$\partial_t \tilde{K} = \beta^c \partial_c \tilde{K} - e^{-4\varphi} g^{ab} \dot{D}_a \dot{D}_b \tilde{\alpha}, \quad (31a)$$

$$\partial_t \tilde{\alpha} = \beta^c \partial_c \tilde{\alpha} - 2\alpha \tilde{K}, \quad (31b)$$

$$\partial_t \tilde{\beta}^a = \beta^c \partial_c \tilde{\beta}^a + \frac{3}{4} \tilde{B}^a, \quad (31c)$$

$$\partial_t \tilde{B}^a = \beta^c \partial_c \tilde{B}^a + g^{bc} \dot{D}_b \dot{D}_c \tilde{\beta}^a + \frac{1}{3} g^{ab} \dot{D}_b \dot{D}_c \tilde{\beta}^c - \frac{4}{3} \alpha g^{ab} \partial_b \tilde{K}. \quad (31d)$$

TABLE II: Coordinate and proper speeds for the vector modes ( $\chi_7$ ,  $\chi_8^\pm$  and  $\chi_9^\pm$ ) and trace-free tensor modes ( $\chi_{10}^\pm$ ) of BSSN with 1+log slicing and gamma-driver shift.

	$\chi_7$	$\chi_8^\pm$	$\chi_9^\pm$	$\chi_{10}^\pm$
coordinate speed	$-\beta^r$	$-\beta^r \pm \sqrt{3g^{rr}}/2$	$-\beta^r \pm \alpha e^{-2\varphi} \sqrt{g^{rr}}$	$-\beta^r \pm \alpha e^{-2\varphi} \sqrt{g^{rr}}$
near trumpet puncture	$-0.53 r$	$-0.53 r \pm 0.87$	$-0.53 r \pm 0.35 r^2$	$-0.53 r \pm 0.35 r^2$
near wormhole puncture	0	$\pm 0.87$	$4.0 r^2$	$4.0 r^2$
proper speed	0	$\pm \sqrt{3} e^{2\varphi} / (2\alpha)$	$\pm 1$	$\pm 1$
near trumpet puncture	0	$2.5/r^2$	$\pm 1$	$\pm 1$
near wormhole puncture	0	$0.22/r^2$	$\pm 1$	$\pm 1$

Here, the fields  $g^{ab}$ ,  $\varphi$ ,  $\alpha$  and  $\beta^a$  are frozen. The principal part of this system coincides with Eqs. (19d,f,g,h). The characteristic fields are  $\chi_4^\pm$  and  $\chi_6^\pm$ . The inverse relations are written in Eqs. (25e,g,h,i).

This system is simple enough to allow us to compute explicitly the time evolution of the characteristic fields, with the following results:

$$\begin{aligned} \partial_t \chi_4^\pm + (-\beta^r \pm e^{-2\varphi} \sqrt{2\alpha g^{rr}}) \partial_r \chi_4^\pm \\ = L_4^\pm(\chi_4) , \end{aligned} \quad (32a)$$

$$\begin{aligned} \partial_t \chi_6^\pm + (-\beta^r \pm \sqrt{g^{rr}}) \partial_r \chi_6^\pm \\ = L_6^\pm(\chi_4, \chi_6) . \end{aligned} \quad (32b)$$

These are the usual advection-type equations plus sources. The sources arise from the fact that the characteristic speeds are not constants. The source functions  $L_4^\pm$  are linear in the characteristic fields  $\chi_4^\pm$  with coefficients that depend on the fixed fields  $g^{ab}$ ,  $\varphi$ ,  $\alpha$ ,  $\beta^a$  and their spatial derivatives. The source functions  $L_6^\pm$  are linear in the characteristic fields  $\chi_4^\pm$  and  $\chi_6^\pm$  with coefficients that depend on the fixed fields  $g^{ab}$ ,  $\varphi$ ,  $\alpha$ ,  $\beta^a$  and their spatial derivatives.

For the full BSSN plus standard gauge system, the time derivatives of  $\chi_4^\pm$  and  $\chi_6^\pm$  include the same terms displayed in Eqs. (32). They will have extra source terms that come from the nonlinearities in the equations. What Eqs.(32) reveal is that, already at the level of the linear system (31), there is coupling between modes  $\chi_4^\pm$  and  $\chi_6^\pm$ . In particular, note that modes  $\chi_4^\pm$  will tend to excite modes  $\chi_6^\pm$ . This coupling plays an important role in the analysis of Section V.

#### IV. CHARACTERISTIC CURVES

Consider a single, spherically symmetric (Schwarzschild) black hole evolved with the puncture method. The initial data is a wormhole in Cartesian coordinates, so the BSSN variables are  $\varphi = \ln(1 + 1/(2r))$ ,  $g_{ab} = \delta_{ab}$ ,  $K = 0$ ,  $A_{ab} = 0$  and  $\Lambda^a = 0$  where  $r = \sqrt{x^2 + y^2 + z^2}$ . The lapse, shift and auxiliary variable are given initial values  $\alpha = 1$ ,  $\beta^a = 0$ , and  $B^a = 0$ . The black hole mass  $M$  is set to unity.

Figures 8 through 11 show the characteristic curves for the various modes from time  $t = 0$  to  $t = 10$ , as the

geometry evolves from wormhole to trumpet. In each figure the dashed curve is the black hole horizon. Figure 8 shows the characteristic curves for  $\chi_4^+$  that begin at time  $t = 0$  at radii  $r = 0.025, 0.05, \dots, 1.0$ . The modes  $\chi_5^+$ ,  $\chi_9^+$ , and  $\chi_{10}^+$  all travel with the speed of light. For these modes Fig. 9 shows the characteristic curves that begin at time  $t = 0$  and radii  $r = 0.025, 0.05, \dots, 1.0$ . Figures 10 and 11 show the characteristic curves for the outgoing, superluminal modes  $\chi_6^+$  and  $\chi_8^+$ , respectively. In both of these figures, one set of curves begin at time  $t = 0$  and radii  $r = 0.025, 0.225, \dots, 0.825$ . Another set of curves begin at radius  $r = 0.025$  and times  $t = 0.2, 0.4, \dots, 4.0$ .

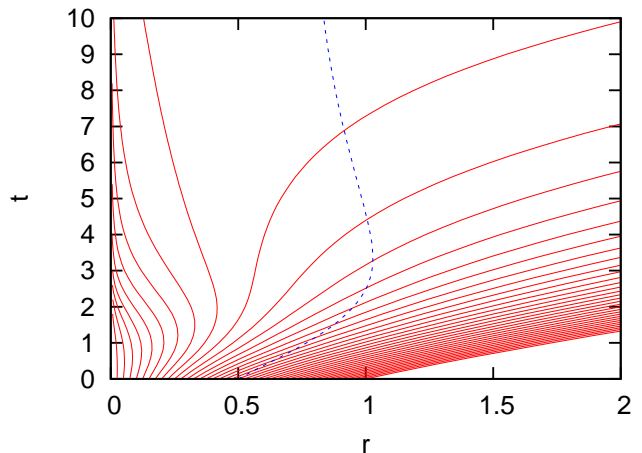


FIG. 8: Characteristic curves for mode  $\chi_4^+$ . The dashed curve is the black hole horizon.

It is clear from these figures that perturbations in modes  $\chi_6^+$  and  $\chi_8^+$  can propagate from the puncture boundary to the black hole exterior. Figure 8 shows that mode  $\chi_4^+$  is also superluminal; however, perturbations within a radius of about  $r \approx 0.2$  do not escape to the outside. This result was observed in Ref. [13].

Tables I and II show that modes  $\chi_4^+$ ,  $\chi_5^+$ ,  $\chi_9^+$ , and  $\chi_{10}^+$  have positive coordinate speeds near the wormhole puncture. This is difficult to see in Figures 8 and 9. What is clear from these figures is that the positive speeds do not last for long. Very quickly, as the geometry shifts from

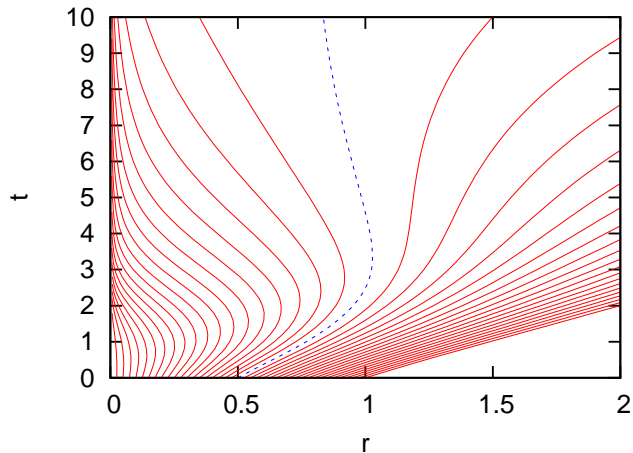
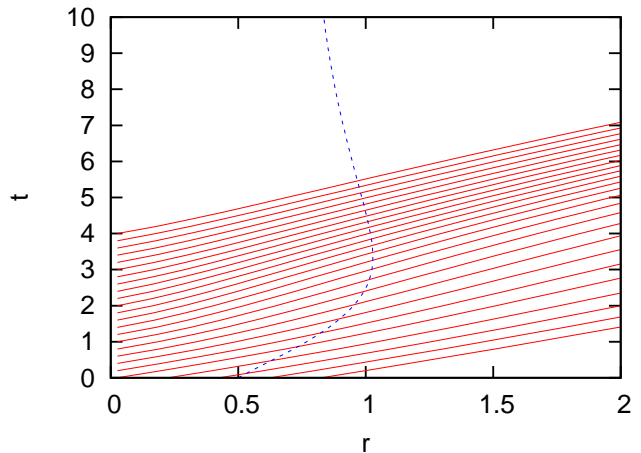
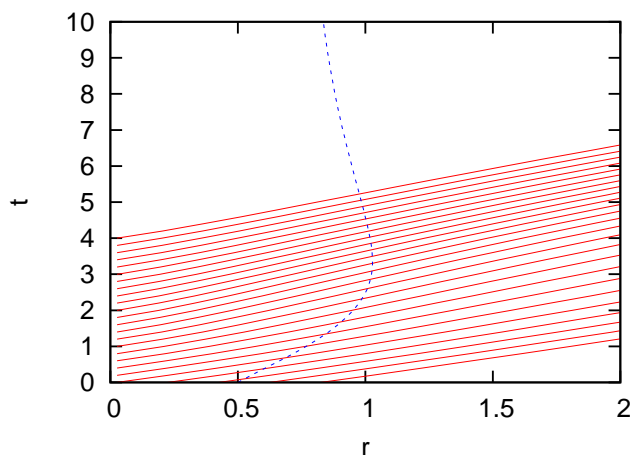
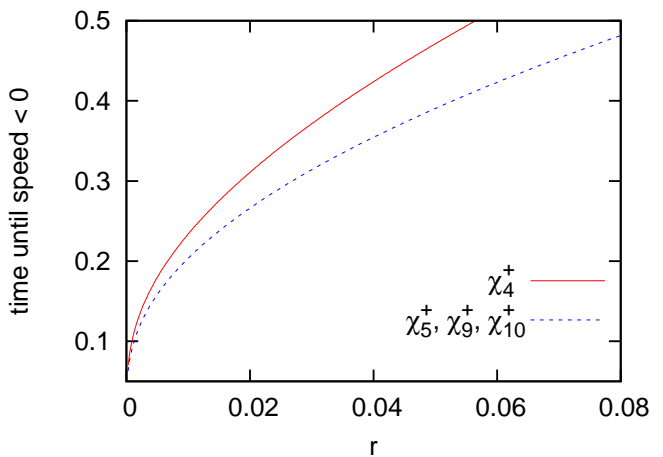
FIG. 9: Characteristic curves for modes  $\chi_5^+$ ,  $\chi_9^+$  and  $\chi_{10}^+$ .FIG. 11: Characteristic curves for mode  $\chi_8^+$ .FIG. 10: Characteristic curves for mode  $\chi_6^+$ .

FIG. 12: Time for characteristic speeds to become negative as a function of the radius.

wormhole to trumpet, the speeds become negative near the puncture. Figure 12 is a graph of the time required for modes  $\chi_4^+$ ,  $\chi_5^+$ ,  $\chi_9^+$ , and  $\chi_{10}^+$  to acquire a negative speed. The time is plotted as a function of  $r$ , which should be viewed as the puncture boundary radius. For example, with a grid spacing of  $h = 1/25$  the puncture boundary has a radius of  $r \approx 1/50 = 0.02$ . Then Fig. 12 shows that mode  $\chi_4^+$  has a positive speed at the puncture boundary up to time  $t \approx 0.3$ . Beyond  $t \approx 0.3$ , the characteristic speed for  $\chi_4^+$  is negative.

In principle, any characteristic mode that can propagate into the computational domain (in our terminology, any mode that is outgoing at the puncture) should be fixed by boundary conditions. Typically, a numerical code that fails to fix such a mode will be unstable. Thus, one would expect that boundary conditions are needed for modes  $\chi_4^+$ ,  $\chi_5^+$ ,  $\chi_9^+$ , and  $\chi_{10}^+$  during the early stages of their evolution. Yet, the puncture evolution scheme does not obviously provide any such boundary conditions. In

practice this does not appear to matter. It seems likely that these modes have positive speeds for such a short amount of time that instabilities do not have a chance to grow. The poor resolution near the puncture boundary might keep the instabilities' growth rates very low.

Consider again a simulation with  $h = 1/25$ . In this case the modes  $\chi_4^+$ ,  $\chi_5^+$ ,  $\chi_9^+$ , and  $\chi_{10}^+$  have positive speeds and are “unfixed” for a time of  $t \approx 0.3$ . If the Courant factor is, say  $1/4$ , then the numerical code will execute about 30 time steps before the speeds change sign. This is perhaps too few time steps for an instability to grow to a significant level.

## V. PERTURBATIONS OF THE TRUMPET GEOMETRY

In this section we carry out simulations of waves reflecting off the puncture boundary of a trumpet black

hole geometry with  $M = 1$ . The simulations assume spherical symmetry and use the cartoon code described in Appendix A. The unperturbed trumpet data is discussed in Appendix B. The perturbations in the BSSN and gauge variables are defined by setting one of the incoming modes to

$$\chi = -0.0008 (r - r_0) e^{-12(r-r_0)^2} \quad (33)$$

and solving Eqs. (25). Here,  $\chi$  is one of  $\chi_1, \chi_2, \chi_3, \chi_4^-, \chi_5^-,$  or  $\chi_6^-$ . Note that the vector and trace-free tensor modes 7 through 10 do not exist in spherical symmetry. Thus, the numerical tests performed here are restricted to modes 1 through 6.

For the incoming modes  $\chi_4^-, \chi_5^-$  and  $\chi_6^-$ , we choose  $r_0 = 10$ . For incoming modes  $\chi_1, \chi_2$  and  $\chi_3$  we use  $r_0 = 4.0$ . In each case we carefully examine the reflections in mode  $\chi_6^+$ . This is the only mode in spherical symmetry that can propagate from the puncture boundary to the black hole exterior.

Let me be specific about the definition of the characteristic fields in spherical symmetry. The definitions (24) include terms such as  $\partial_n \tilde{g}_{nn}$ , which is shorthand notation for  $n^a \partial_a (\tilde{g}_{bc} n^b n^c)$ . The normal vector orthogonal to the  $r = \text{const}$  coordinate surfaces is  $n^a = g^{ar} / \sqrt{g^{rr}}$ , which simplifies to  $\delta_r^a / \sqrt{g_{rr}}$  in spherical symmetry. Thus, we have

$$\partial_n \tilde{g}_{nn} = \partial_r (\tilde{g}_{rr} / g_{rr}) / \sqrt{g_{rr}}, \quad (34a)$$

$$\partial_n \tilde{g}_{AA} = 2 \partial_r (\tilde{g}_{\theta\theta} / g_{\theta\theta}) / \sqrt{g_{rr}}, \quad (34b)$$

$$\tilde{A}_{nn} = \tilde{A}_{rr} / g_{rr}, \quad (34c)$$

$$\partial_n \tilde{\varphi} = (\partial_r \tilde{\varphi}) / \sqrt{g_{rr}}, \quad (34d)$$

$$\tilde{K} = \tilde{K}, \quad (34e)$$

$$\tilde{\Lambda}^n = \sqrt{g_{rr}} \tilde{\Lambda}^r, \quad (34f)$$

$$\partial_n \tilde{\alpha} = (\partial_r \tilde{\alpha}) / \sqrt{g_{rr}}, \quad (34g)$$

$$\partial_n \tilde{\beta}^n = \partial_r (\sqrt{g_{rr}} \tilde{\beta}^r) / \sqrt{g_{rr}}, \quad (34h)$$

$$\tilde{B}^n = \sqrt{g_{rr}} \tilde{B}^r. \quad (34i)$$

where  $\theta$  is the usual polar angle in spherical coordinates. In the cartoon code described in Appendix A, the modes (24) are defined by using the frozen coefficients approximation to remove factors of the unperturbed fields  $g_{rr}$  and  $g_{\theta\theta}$  from the derivatives in Eqs. (34). For example, in Eqs. (24) and (25), the term  $\partial_n \tilde{g}_{nn}$  is approximated by  $(\partial_r \tilde{g}_{rr}) / (g_{rr})^{3/2}$ .

The figures throughout this section use the following convention: The curves (solid or dashed, with various patterns) are obtained from simulations at resolution  $h = 1/100$ . The data points (dots or crosses or other symbols) are obtained from simulations at resolution  $h = 1/50$ . Unless otherwise stated, only every fifth data point is displayed for the lower resolution case.

### A. Incident mode $\chi_6^-$

Figure 13 shows a perturbation in mode  $\chi_6^-$  at time  $t = 3.4$ . This pulse propagates inward toward the puncture  $r = 0$ . Figure 14 shows the incident pulse at  $t = 8.0$ , just before it hits the puncture boundary. Figures 15 and 16 show the reflected pulse  $\chi_6^+$  propagating outward at times 11.4 and 16.0, respectively. In each of these four figures, the dots (every fifth data point from a simulation with  $h = 1/50$ ) lie on top of the solid curve (from a simulation with  $h = 1/100$ ). These results are convergent. In particular, the reflected wave pulse does *not* show any resolution-dependent time delay.

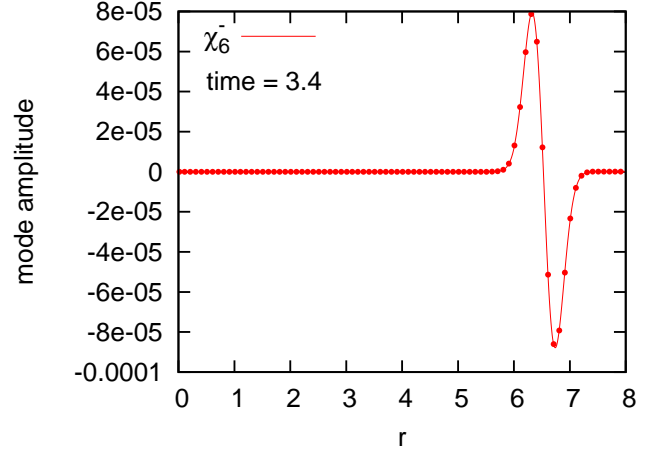


FIG. 13: Incoming mode  $\chi_6^-$  at time 3.4. (The initial excitation is in  $\chi_6^-$ .)

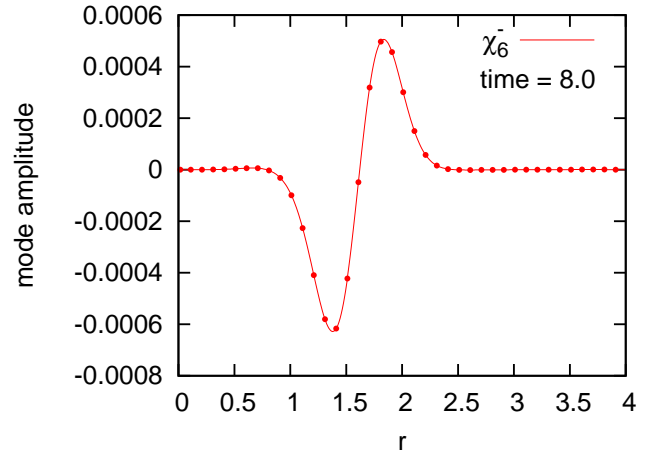


FIG. 14: Incoming mode  $\chi_6^-$  at time 8.0. (The initial excitation is in  $\chi_6^-$ .)

It is informative to compare the amplitudes of the incoming and reflected pulses. From Fig 13 we see that the incident mode  $\chi_6^-$  has amplitude  $A \sim 8 \times 10^{-5}$  at  $t = 3.4$ .

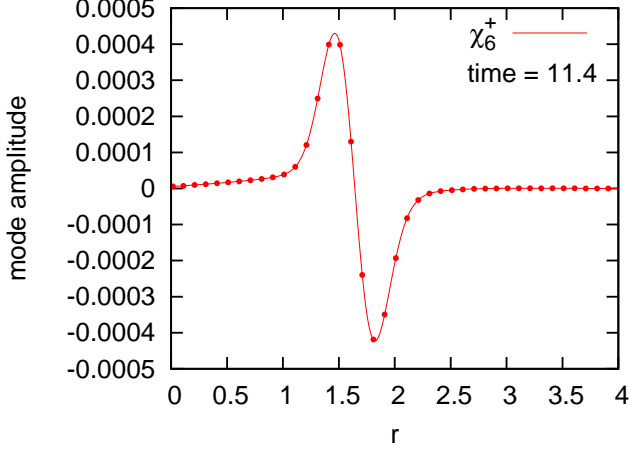


FIG. 15: Outgoing mode  $\chi_6^+$  at time 11.4. (The initial excitation is in  $\chi_6^-$ .)

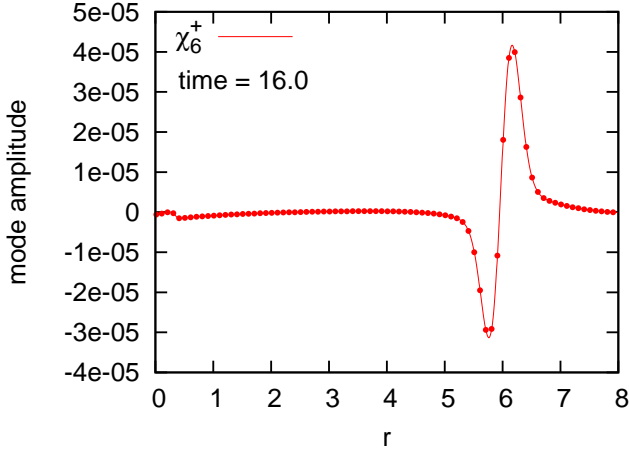


FIG. 16: Outgoing mode  $\chi_6^+$  at time 16.0. (The initial excitation is in  $\chi_6^-$ .)

By  $t = 8.0$  the amplitude has grown by almost an order of magnitude to  $A \sim 6 \times 10^{-4}$ . It continues to grow as the pulse approaches the puncture. The reflected mode  $\chi_6^+$  initially has a very large amplitude. It drops rapidly to  $A \sim 4 \times 10^{-4}$  at time  $t = 11.4$ , as shown in Fig. 15. By  $t = 16.0$  it has dropped an order of magnitude to  $A \sim 4 \times 10^{-5}$ . At equal distances from the puncture (say,  $r \approx 6.0$ ), the reflected pulse is almost as large as the incident pulse.

The small step in the data for  $\chi_6^+$  seen in Fig 16 at  $r \approx 0.4$  deserves some discussion. To begin, let us consider the modes  $\chi_4^\pm$ ,  $\chi_5^\pm$  and  $\chi_6^\pm$  before the pulse  $\chi_6^-$  hits the puncture boundary. Figure 17 displays these modes at time  $t = 8.0$ . If our system of partial differential equations were linear with constant wave speeds, these modes would not be excited at all. However, due to the nonlinear nature of Einstein's theory, these modes build in am-

plitude as the initial pulse  $\chi_6^-$  propagates inward. Even the modes  $\chi_4^+$ ,  $\chi_5^+$  and  $\chi_6^+$ , which are normally outgoing, develop nontrivial profiles that are carried inward along with  $\chi_6^-$ . The largest of these modes is  $\chi_5^+$ , with an amplitude  $A \sim 1 \times 10^{-4}$ . However, keep in mind that relative amplitudes among the different modes have little meaning since the normalization of the modes is arbitrary.

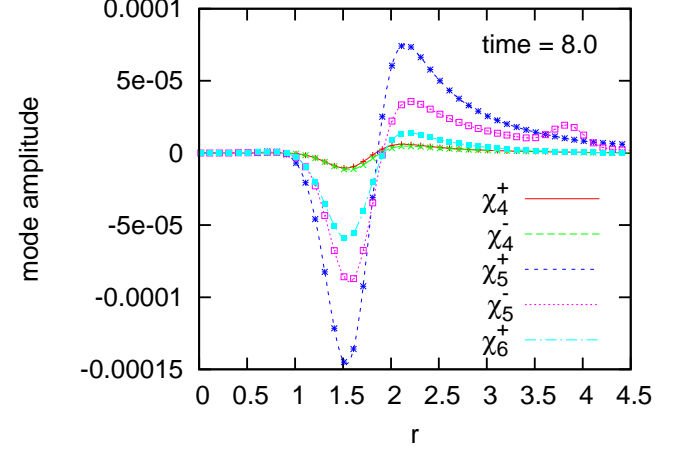


FIG. 17: Modes  $\chi_4^\pm$ ,  $\chi_5^\pm$ , and  $\chi_6^+$  at time 8.0, carried inward along with the initially excited mode  $\chi_6^-$ . Compare with Fig. 14.

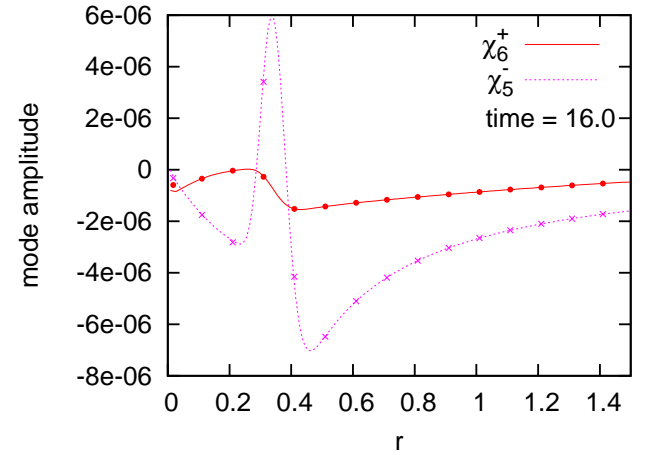


FIG. 18: Modes  $\chi_5^-$ , and  $\chi_6^+$  at time 16.0. These waveforms are traveling inward. (The initial excitation is in  $\chi_6^-$ .)

The important feature of Fig. 17 is the small hump in  $\chi_5^-$  that peaks at about  $r = 3.8$ . This hump is initially part of the larger perturbation in  $\chi_5^-$  that is carried along with  $\chi_6^-$ . However, mode  $\chi_5^-$  naturally tends to move more slowly than  $\chi_6^-$ , as seen from the data in Table I. By  $t = 8.0$  a small piece of  $\chi_5^-$  has broken free from the other perturbations and fallen behind. It continues to propagate inward, moving more and more slowly as it

approaches the puncture. Figure 18 shows the hump in  $\chi_5^-$  at  $t = 16.0$ , just before it reaches the puncture. That figure includes a plot of  $\chi_6^+$ . We see that the nonlinear couplings have created a new perturbation in  $\chi_6^+$ , that is carried inward along with  $\chi_5^-$ . This perturbation in  $\chi_6^+$  is seen as a small step at  $r \approx 0.4$  in both Figs. 16 and 18. Note that these features are all convergent.

Finally, let us compare the incoming pulses  $\chi_6^-$  at  $t = 3.4$  and  $t = 8.0$ ; these are pictured in Figs. 13 and 14. Observe that the pulse at  $t = 8.0$  is inverted relative to the pulse at  $t = 3.4$ . This is related to the breakdown in hyperbolicity that occurs when  $(1 - 2\alpha e^{-4\varphi}) = 0$ . In particular, the factor  $(1 - 2\alpha e^{-4\varphi})$  appears in Eq. (24f) for  $\chi_6^\pm$  and in the denominators of several terms in the inverse relations (25). This factor vanishes at  $r = 4.06$  for the trumpet geometry. More precisely,  $(1 - 2\alpha e^{-4\varphi})$  is positive for  $r < 4.06$  and negative for  $r > 4.06$ . Thus, as the pulse  $\chi_6^-$  passes through  $r = 4.06$ , the factors  $(1 - 2\alpha e^{-4\varphi})$  in its definition (24f) change sign. This change of sign is responsible for the inversion that is seen in the incoming pulse  $\chi_6^-$ . Figure 19 shows a time sequence of the inversion process. One can see from Figs. 15 and 16

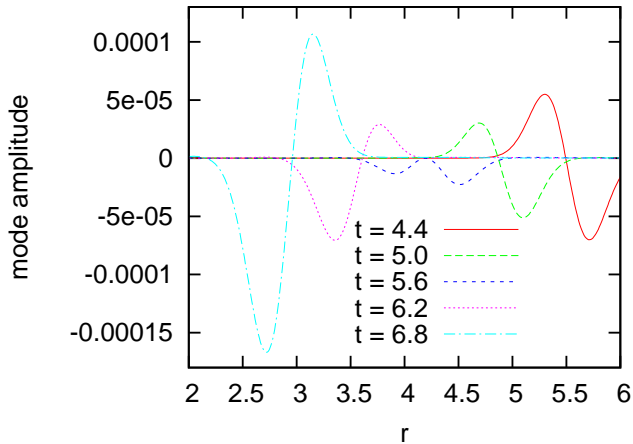


FIG. 19: Time sequence showing mode  $\chi_6^-$  as it travels inward through the point  $r = 4.06$  where hyperbolicity breaks down.

that a similar inversion occurs in the reflected pulse  $\chi_6^+$  as it travels outward and passes through  $r = 4.06$ .

### B. Incident mode $\chi_4^-$

Figures 20 and 21 show the initial pulse  $\chi_4^-$  propagating inward at times  $t = 7.0$  and  $t = 11.0$ , respectively. Figures 22 and 23 show a reflection in  $\chi_6^+$  propagating outward at times  $t = 11.0$  and  $t = 15.0$ , respectively. All of these figures show nice convergence, with no resolution-dependent time delay.

These results require further analysis and explanation. Note that the pulse  $\chi_6^+$ , shown in Fig. 22, emerges from the puncture region *before* the incident pulse  $\chi_4^-$  reaches

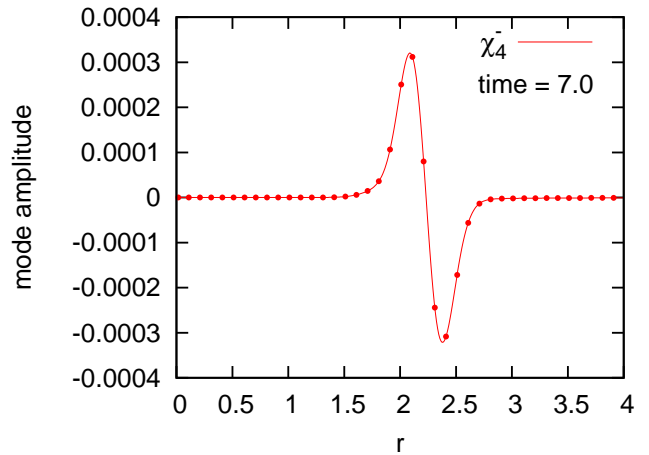


FIG. 20: Incoming mode  $\chi_4^-$  at time 7.0. (The initial excitation is in  $\chi_4^-$ .)

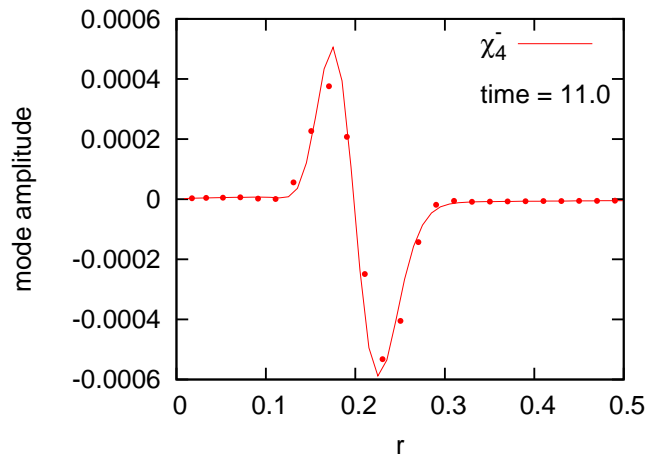


FIG. 21: Incoming mode  $\chi_4^-$  at time 11.0. The dots coincide with all of the data points for the low resolution simulation. (The initial excitation is in  $\chi_4^-$ .)

the puncture boundary. Figure 21 shows that at time  $t = 11.0$ , the incident pulse is at  $r \approx 0.2$ . Evidently the perturbation in the outgoing mode  $\chi_6^+$  is caused by something other than a reflection of  $\chi_4^-$  from the puncture boundary.

In Fig. 24 we plot the modes  $\chi_4^+$ ,  $\chi_5^\pm$ , and  $\chi_6^\pm$  at time  $t = 7.0$ . What is immediately clear from this figure is that the nonlinear interactions have produced a large excitation in  $\chi_6^-$ . Observe that even with the “gauge system” described in Sec. III.D, the spatial variations in the characteristic speeds will introduce a source in the evolution equation for  $\chi_6^-$  that depends on  $\chi_4^-$ . This is a particularly strong coupling; note that the amplitude of  $\chi_6^-$  at  $t = 7.0$  is several times larger than the amplitude of  $\chi_4^-$ . (Recall, however, that relative amplitudes depend on the normalization of the modes.)

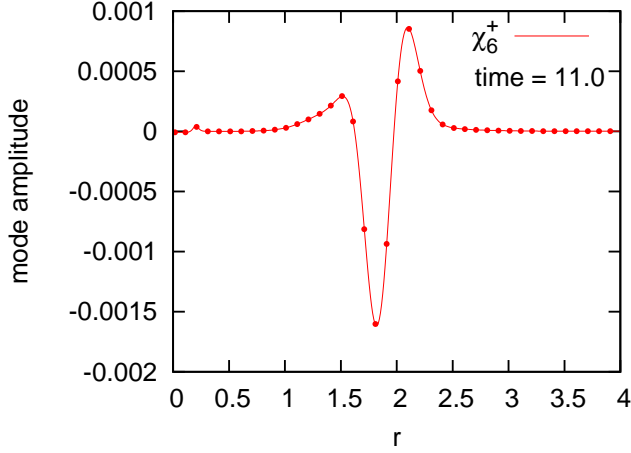


FIG. 22: Outgoing mode  $\chi_6^+$  at time 11.0. (The initial excitation is in  $\chi_4^-$ .)

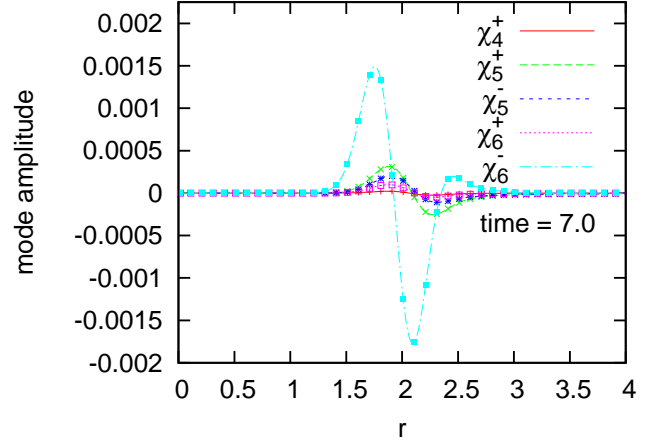


FIG. 24: Modes  $\chi_4^+$ ,  $\chi_5^\pm$ , and  $\chi_6^\pm$  at time 7.0. These modes are carried inward along with the initially excited mode  $\chi_4^-$ . Compare with Fig. 20.

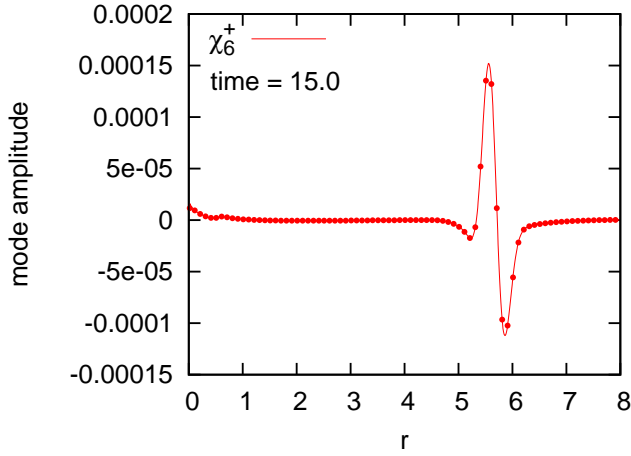


FIG. 23: Outgoing mode  $\chi_6^+$  at time 15.0. (The initial excitation is in  $\chi_4^-$ .)

Table I shows that near the puncture, mode  $\chi_6^-$  propagates more quickly than mode  $\chi_4^-$ . As a consequence the excitation in  $\chi_6^-$  races ahead of  $\chi_4^-$ . One can see this already at time  $t = 7.0$ ;  $\chi_6^-$  is centered at  $r \approx 1.9$  while  $\chi_4^-$  is centered at  $r \approx 2.2$ . The large perturbation in  $\chi_6^-$  reaches the puncture boundary at  $t \approx 9.0$  and produces the large reflection in mode  $\chi_6^+$ , seen in Figs. 22 and 23.

By time  $t = 11.0$ , the incident pulse  $\chi_4^-$  has reached  $r \approx 0.5$ . Observe that at  $t = 11.0$ , Fig. 22 shows a small hump in  $\chi_6^+$  near  $r \approx 0.5$ . This hump is caused by the coupling between modes  $\chi_4^-$  and  $\chi_6^+$ . The tail of this hump is seen in Fig. 23 as an upturn in the data near the origin at  $t = 15.0$ .

Figure 25 shows a close-up view of  $\chi_6^+$  near  $r = 0$  at  $t = 15.0$ . This view reveals another feature, a bump in  $\chi_6^+$  that peaks around  $r \approx 0.6$ . Close inspection of the data shows that this bump has the following origin: The

main reflection in  $\chi_6^+$  creates an excitation in mode  $\chi_5^-$ , which then propagates inward toward the origin. In turn, this incoming wave  $\chi_5^-$  creates a distortion in  $\chi_6^+$  that is carried inward along with  $\chi_5^-$ . It is this distortion that appears as the small bump in Fig. 25.

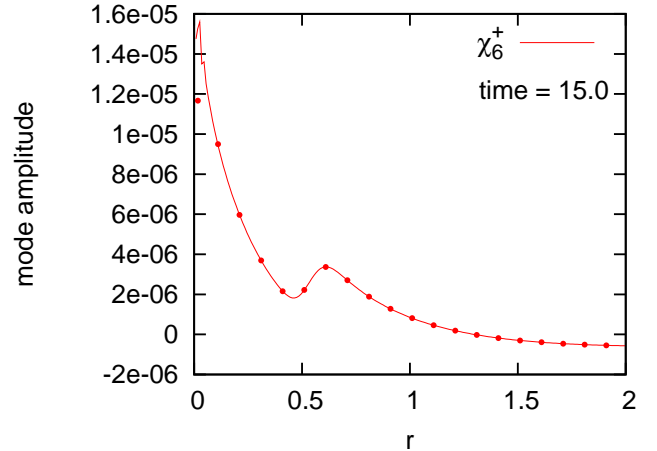


FIG. 25: Close-up view of outgoing mode  $\chi_6^+$  at time 15.0. Compare with Fig. 23. (The initial excitation is in  $\chi_4^-$ .)

The incident perturbation  $\chi_4^-$  reaches the puncture boundary at about  $t \approx 15.0$ . It does not produce a significant reflection in mode  $\chi_6^+$ . Figure 26 shows the data for  $\chi_6^+$  at  $t = 19.0$ , when such a reflection would be expected to appear in the range  $0 < r < 4.0$ . By this time the excitation in  $\chi_6^+$  has decayed to a “tail” near the boundary that oscillates as it flattens to zero. Note that the amplitude in Fig. 26 is quite small compared to the earlier reflections shown in Figs. 22 and 23. More importantly, the results are convergent: there are no resolution-dependent features.

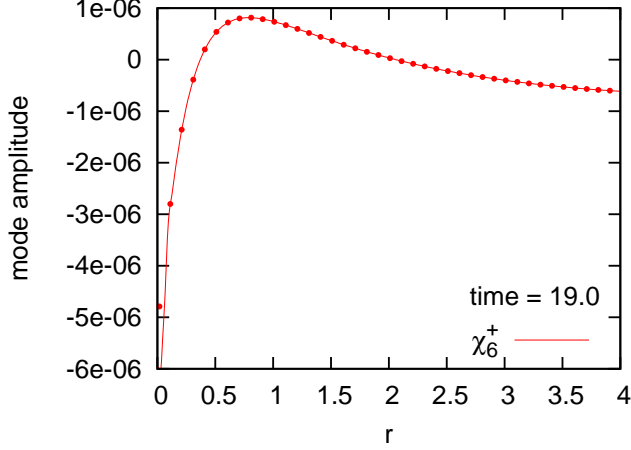


FIG. 26: Outgoing mode  $\chi_6^+$  at time 19.0. (The initial excitation is in  $\chi_4^-$ .)

### C. Incident mode $\chi_5^-$

Figure 27 shows the mode  $\chi_5^-$  at time  $t = 11.0$  as it propagates inward toward the puncture boundary. Non-linear interactions cause the other modes to become excited. By  $t = 7.0$ , mode  $\chi_6^-$  has been excited to an amplitude of about  $A \approx 1 \times 10^{-5}$ . This mode moves more quickly than  $\chi_5^-$  and reaches the puncture at  $t \approx 9.0$ .

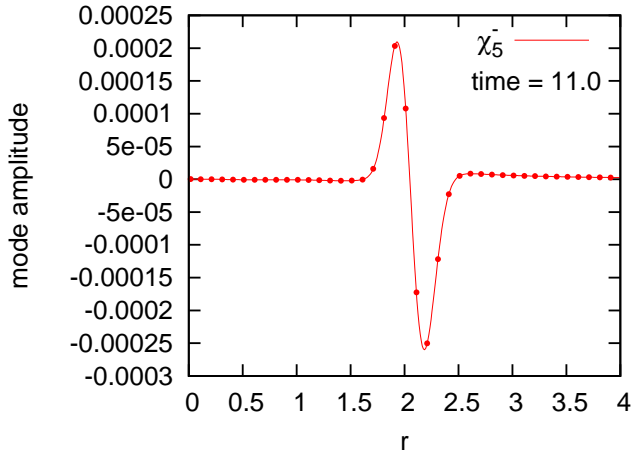


FIG. 27: Incoming mode  $\chi_5^-$  at time 11.0. (The initial excitation is in  $\chi_5^-$ .)

The modes  $\chi_4^\pm$ ,  $\chi_5^\pm$ , and  $\chi_6^\pm$  are plotted in Fig. 28 at time  $t = 11.0$ . The relatively large perturbation in  $\chi_6^+$ , with amplitude  $A \approx 1 \times 10^{-5}$ , comes from the earlier reflection of  $\chi_6^-$ . This mode is moving outward at  $t = 11.0$ , and is convergent. The other modes shown in Fig. 28 are moving inward, being carried by the initial perturbation  $\chi_5^-$ .

The main pulse  $\chi_5^-$  reaches the puncture boundary at

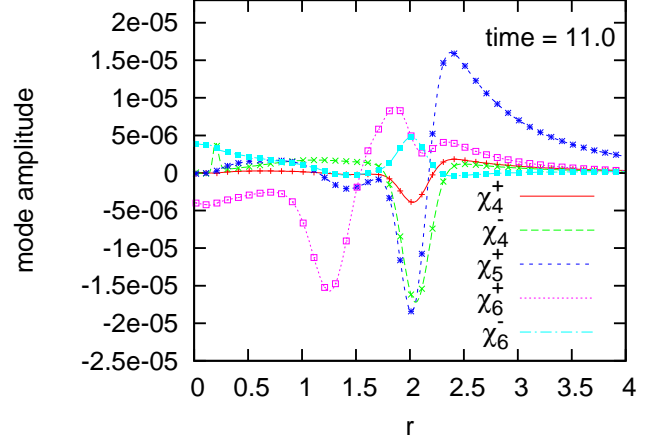


FIG. 28: Modes  $\chi_4^\pm$ ,  $\chi_5^\pm$ , and  $\chi_6^\pm$  at time 11.0. The mode  $\chi_6^+$  is moving outward. The other modes are moving inward along with the initial perturbation in  $\chi_5^-$ .

about  $t \approx 20.0$ . It does not produce a distinct reflection in mode  $\chi_6^+$ . Figure 29 shows mode  $\chi_6^+$  at  $t = 22.0$ , when such a reflection would appear in the range  $0 < r < 4.0$ . The only excitation in  $\chi_6^+$  at this time is a decaying tail, similar to the profile seen at late times when the initial perturbation is in  $\chi_4^-$ ; see Fig. 26. This tail is convergent, showing no resolution dependence.

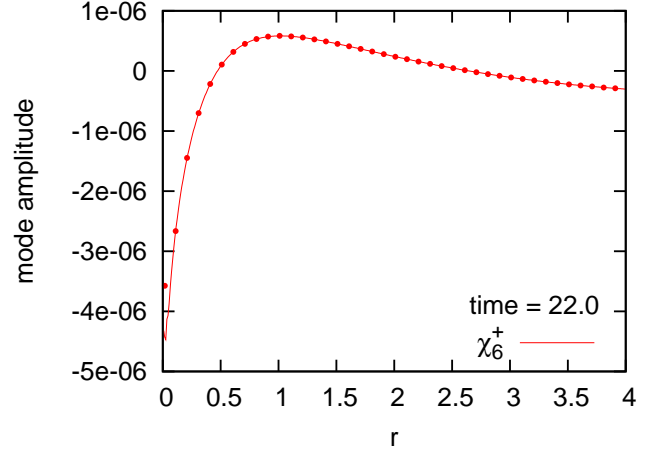


FIG. 29: Outgoing mode  $\chi_6^+$  at time 22.0. (The initial excitation is in  $\chi_5^-$ .)

### D. Incident modes $\chi_1$ , $\chi_2$ and $\chi_3$

The results of these three cases are qualitatively very similar to one another. The incident pulse takes about  $t \approx 45$  to propagate from its initial location at  $r_0 = 4.0$  to the puncture boundary. Long before that, the non-linear interactions create excitations in the other modes.

In particular, the excitation in mode  $\chi_6^-$  races ahead and reaches the puncture boundary at  $t \approx 4$ . As expected, this produces a reflection in mode  $\chi_6^+$  that propagates outward to the black hole exterior. When the initial perturbations in  $\chi_1$ ,  $\chi_2$  or  $\chi_3$  hit the puncture boundary, they do not appear to couple to any other modes. At late times we only see a residual tail in  $\chi_6^+$  that decays in time.

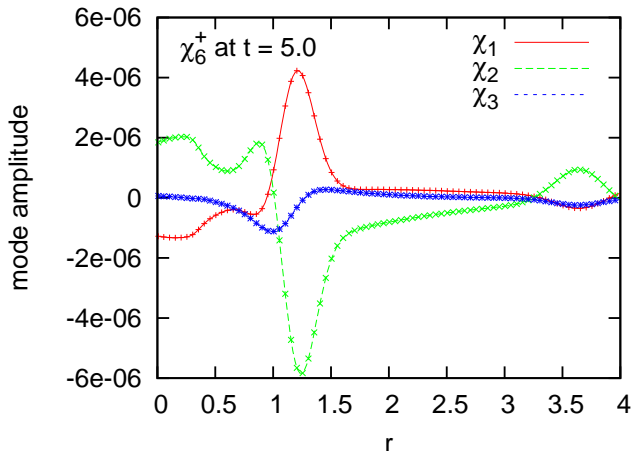


FIG. 30: Mode  $\chi_6^+$  at time 5.0. The three curves correspond to initial excitations in  $\chi_1$ ,  $\chi_2$  and  $\chi_3$ .

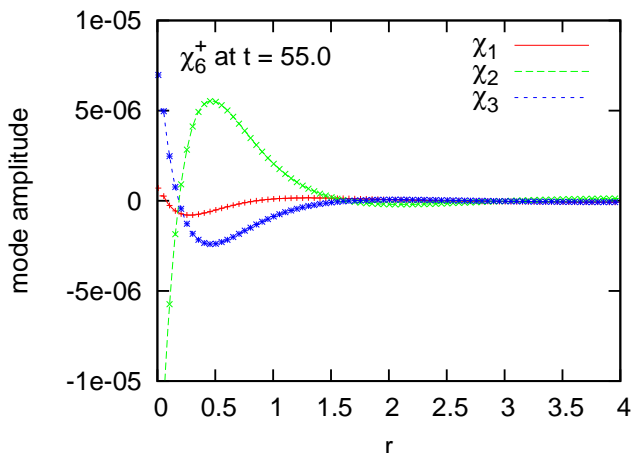


FIG. 31: Mode  $\chi_6^+$  at time 55.0. The three curves correspond to initial excitations in  $\chi_1$ ,  $\chi_2$  and  $\chi_3$ .

Figure 30 shows  $\chi_6^+$  for the three cases with initial excitations in  $\chi_1$ ,  $\chi_2$  and  $\chi_3$  at time  $t = 5.0$ . The large pulses near  $r = 1.2$  are reflections from  $\chi_6^-$ . These wave forms are traveling outward with positive speed. The smaller pulses near  $r = 3.6$  are excitations that are carried inward along with the initial perturbations in  $\chi_1$ ,  $\chi_2$  or  $\chi_3$ . None of these curves show any resolution dependence. As the initial perturbation passes through the puncture

boundary, the mode  $\chi_6^+$  develops a relatively large amplitude profile. That profile decays in time, and does not appear to propagate outward. In Fig. 31 we see  $\chi_6^+$  at time  $t = 55$ , after the initial pulse has hit the puncture boundary. This figure shows the residual profile and no resolution dependence.

## VI. INTERPRETATION AND DISCUSSION

Only the modes  $\chi_6^+$  and  $\chi_8^+$  are able to propagate from the puncture boundary to the black hole exterior. When starting the evolution from a wormhole configuration, modes  $\chi_4^+$ ,  $\chi_5^+$ ,  $\chi_9^+$  and  $\chi_{10}^+$  are outgoing at the puncture boundary. However, these modes quickly acquire negative speeds near the boundary and their characteristic curves never extend from the puncture boundary to the black hole exterior.

The modes  $\chi_6^\pm$  and  $\chi_8^\pm$  have constant speeds,  $\pm\sqrt{g^{rr}} \approx \pm 1$  and  $\pm\sqrt{3g^{rr}}/2 \approx \pm 0.87$  respectively, near the puncture boundary of a trumpet geometry. This implies that these modes propagate between the puncture boundary and the black hole exterior with no resolution dependence. These modes do not recognize that the puncture boundary moves when the resolution is changed. In effect, *modes  $\chi_6^\pm$  and  $\chi_8^\pm$  propagate in the conformal geometry, not the physical geometry.*

The other modes, namely  $\chi_1$ ,  $\chi_2$ ,  $\chi_3$ ,  $\chi_4^\pm$ ,  $\chi_5^\pm$ ,  $\chi_7$ ,  $\chi_9^\pm$  and  $\chi_{10}^\pm$ , have speeds  $-\beta^r \approx -0.53r$  near the puncture. They propagate in the physical geometry. These modes are affected by the movement of the puncture boundary when the resolution is changed. Once the spatial slice settles to a trumpet geometry, all of these modes are incoming at the puncture boundary.

The distinction between modes that propagate in the physical geometry and those that propagate in the conformal geometry can be understood by examining the speeds from Tables I and II. The coordinate speeds for modes  $\chi_6^\pm$  and  $\chi_8^\pm$  are built from the shift vector and the conformal metric component  $g^{rr}$ . The physical metric does not appear. On the other hand, the coordinate speeds for modes  $\chi_4^\pm$ ,  $\chi_5^\pm$ ,  $\chi_9^\pm$  and  $\chi_{10}^\pm$  are built from the shift vector and the physical metric component  $e^{-4\varphi}g^{rr}$ .

The time required for a perturbation in any mode to travel between the puncture boundary at  $r \approx h/2$  and a finite radius  $r_0$  is

$$T \approx \int_{h/2}^{r_0} \frac{dr}{|v|}, \quad (35)$$

where  $v$  is the coordinate speed. For the modes that propagate in the conformal geometry,  $v$  is constant near the puncture boundary and  $T$  depends linearly on the grid resolution  $h$ . In the limit  $h \rightarrow 0$ , this dependence drops out. In this sense, the propagation time does not depend on resolution. For the modes that propagate in the physical geometry,  $v$  behaves like  $|v| \sim r$  near the puncture boundary of a trumpet. For these modes  $T$  diverges like  $|\ln(h)|$ . As the resolution is increased  $h$  is

decreased and the puncture boundary is pushed farther down the trumpet throat. The propagation time  $T$  goes to infinity.

Once the wormhole has evolved into a trumpet, all of the modes that propagate in the physical geometry have negative speeds at the puncture boundary. The concern is that a disturbance in one of these modes could propagate inward to the puncture boundary where it might couple to one of the outgoing superluminal modes  $\chi_6^+$  or  $\chi_8^+$ . Since the time required for the initial disturbance to reach the puncture boundary is resolution dependent, the reflection would be delayed in time as the resolution is increased.

The numerical experiments in Sec. V suggest that there is no coupling at the puncture boundary between the modes that propagate in the physical geometry and the modes that propagate in the conformal geometry. These experiments were limited to spherical symmetry, so not all possible couplings could be tested.

The lack of coupling between the two types of modes can be understood by considering the finite differencing stencil as it appears from the perspectives of the conformal and physical geometries. From the point of view of the physical geometry, the finite differencing stencil is one sided at the puncture boundary. We can see this in Fig. 2. For any point on the puncture boundary, the legs of a stencil will always extend outward (into the computational domain). For the modes that travel in the physical geometry, the puncture method correctly avoids placing any boundary conditions at the puncture boundary by using one-sided stencils. These modes are simply advected through the puncture boundary and off the computational domain.

For the modes that travel in the conformal geometry, the finite differencing stencils appear as standard stencils that surround the origin of a computational grid in  $R^3$ . For these modes, there is no boundary and the puncture method correctly treats the puncture like any other point in the computational domain.

Because the modes  $\chi_6^\pm$  and  $\chi_8^\pm$  propagate in the conformal geometry, which is smooth at the origin, we expect the puncture method to impose some type of smoothness conditions at  $r = 0$ . It is not entirely clear what those conditions might be since the unperturbed fields are not all smooth at that point. The following observations are suggestive. If we assume that the perturbations in the vector fields  $B^a$  and  $\beta^a$  are smooth at the origin, then we must have  $\tilde{B}^n = 0$  and  $\tilde{\beta}^n = 0$ . From Eq. (24f) we see that the modes  $\chi_6^\pm$  obey  $\chi_6^\pm(0) = \mp \partial_n \tilde{\beta}^n(0)$  at  $r = 0$  for a trumpet geometry. Thus, we expect that the relation

$$\chi_6^+(0) + \chi_6^-(0) = 0 \quad (36)$$

should hold for all of the simulations in Sec. V. A close inspection of the data shows that this is indeed the case.

For BSSN with standard gauge conditions, some modes effectively propagate in the physical geometry and some effectively propagate in the conformal geometry. In light

of this understanding, let us examine the scalar field example of Sec. II. In that case the characteristic speeds are  $v = \pm r/\sqrt{1+r^2} \approx \pm r$  near the puncture boundary. Both the incoming and outgoing modes propagate in the physical geometry. The time  $T$  for these modes to travel between the puncture boundary and any finite location diverges like  $|\ln(h)|$ . Moreover, the finite difference stencil for both of these modes is one sided at the puncture boundary. This is bad. For a properly constructed numerical code, the outgoing mode (the mode that is propagating into the computational domain) should be fixed by boundary conditions. This does not happen when we naively apply the puncture method as in Sec. II. Correspondingly, the code used in Sec. II does not work—the simulations do not converge to a continuum solution as the resolution is increased.

On the other hand, a properly constructed numerical code for BSSN with standard gauge should have precisely the properties of the puncture method. That is, the code should use something like one-sided finite difference stencils for the modes that propagate in the physical geometry, since all of these modes are incoming at the puncture boundary. For the modes that propagate in the conformal geometry there is no boundary, so the code should use the same stencils near the origin as elsewhere.

The analysis in this paper assumes that the gamma-driver shift condition includes all advection terms. There are three such terms, one in Eq. (10g) and two in Eqs. (10h). Let me comment on the cases in which one or more advection terms are omitted. What we look for is a case with an outgoing mode whose coordinate speed goes to zero at the puncture. To determine the speeds near the puncture boundary, I will assume that the geometry evolves to a stationary trumpet with  $\alpha \approx ar$ ,  $\beta^r \approx br$ ,  $g^{rr} \approx g$  and  $\varphi \approx -\ln(pr)/2$  near the puncture boundary, where  $a$ ,  $b$ ,  $g$  and  $p$  are all constants. This assumption holds if we include all advection terms, and it holds if we include no advection terms.

With the assumption above, there is only one scalar mode and one vector mode whose speeds can approach zero through positive values near  $r = 0$ . This happens when the second advection term in Eq. (10h) is dropped but the other advection terms are kept. [The second advection term is contained in  $(\partial_t \Lambda^a)_{\text{rhs}}$ .] In that case the scalar mode has speed  $b^3 r^3/g$  and the vector mode has speed  $4b^3 r^3/(3g)$  near the puncture boundary. If either of these modes is excited at the puncture boundary, it will propagate to the black hole exterior with a resolution-dependent time delay. More precisely, the propagation time will diverge like  $1/h^2$  as the resolution is increased. The conclusion is that we should not drop the second advection term in the gamma-driver shift equation Eq. (10h) unless one or both of the other advection terms are dropped as well.

## APPENDIX A: CARTOON BSSN CODE

The cartoon code evolves the BSSN plus standard gauge system in spherical symmetry using Cartesian finite difference stencils. The computational grid is shown in Fig. 32. The puncture is at the origin. The physical grid consists of the single line of grid points at  $x/h = y/h = 1/2$  and  $z/h = 1/2, 3/2, \dots$ , where  $h$  is the grid spacing. These points are shown as solid dots in the figure. The open circles represent buffer points,

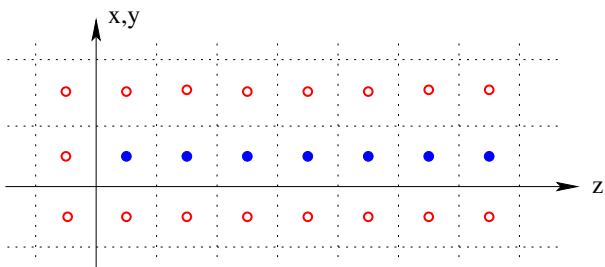


FIG. 32: Grid for the cartoon code. The physical grid points are filled dots, and buffer points are open circles.

which are needed for computing finite difference derivatives. The figure shows one layer of buffer points; the actual code uses two layers of buffer points.

The buffer points are filled by spherical symmetry using known values of the fields at physical grid points. Consider a scalar field such as the lapse function  $\alpha$ . The value of  $\alpha$  at a buffer point  $(x_g, y_g, z_g)$  is found by considering the coordinate distance from the origin:  $r_g = \sqrt{x_g^2 + y_g^2 + z_g^2}$ . We compute the value of  $z$  along the physical grid line for the point at radius  $r_g$ . That is, we set  $\sqrt{(h/2)^2 + (h/2)^2 + z^2} = r_g$  and solve for  $z$ ; this gives

$$z = \sqrt{x_g^2 + y_g^2 + z_g^2 - h/2}. \quad (\text{A1})$$

I use an eighth-order interpolation along the  $z$  direction to find  $\alpha$  at radius  $r_g$ .

As an example, consider the buffer point  $(5h/2, 3h/2, 9h/2)$ . According to Eq. (A1) we have  $z = 5.315h$ . Thus, the point  $(h/2, h/2, 5.315h)$  lies along the physical grid line at the same radius as the buffer point. Note that  $z = 5.315h$  lies between  $9h/2$  and  $11h/2$ . The value of  $\alpha$  at  $(h/2, h/2, 5.315h)$  is found by interpolation over the eight physical points with  $z/h = 3/2, \dots, 17/2$ . This is the value assigned to  $\alpha$  at the buffer point.

The conformal connection  $\Lambda^a$ , the shift  $\beta^a$ , and the auxiliary field  $B^a$  are all spatial vectors. Let  $V^a$  denote one of these vectors. In spherical symmetry, the Cartesian components of any vector field can be written as

$$V^a = S(r) \frac{x^a}{r}, \quad (\text{A2})$$

where  $S(r)$  is a scalar field. Here,  $x^a$  are Cartesian coordinates and  $r = \sqrt{x^2 + y^2 + z^2}$ . Relation (A2) can be inverted,

$$S = V^a \frac{x_a}{r}, \quad (\text{A3})$$

where indices on  $x^a$  are lowered with the flat Cartesian metric  $\delta_{ab}$ . In filling buffer points for vectors, we first apply Eq. (A3) to compute the scalar  $S$ . Next, we apply the scheme outlined above to fill the buffer points for  $S$ . Finally, the buffer points for  $V^a$  are computed from Eq. (A2).

Let  $T_{ab}$  denote one of the symmetric tensor fields  $g_{ab}$  or  $A_{ab}$ . In spherical symmetry we have

$$T_{ab} = P(r) \frac{x_a x_b}{r^2} + Q(r) \delta_{ab}, \quad (\text{A4})$$

where  $P$  and  $Q$  are scalars. This relation can also be expressed as

$$T_{ab} dx^a dx^b = (P + Q) dr^2 + r^2 Q d\Omega^2, \quad (\text{A5})$$

where  $d\Omega^2$  is the metric on the unit sphere. Buffer points for  $T_{ab}$  are filled by first computing the scalars from the inverse relations

$$P + 3Q = T_{ab} \delta^{ab}, \quad (\text{A6a})$$

$$P + Q = T_{ab} \frac{x^a x^b}{r^2}. \quad (\text{A6b})$$

We then fill the buffer points for the scalars, as outlined above. Finally we apply Eq. (A4) to obtain buffer point values for  $T_{ab}$ .

Note that the calculations discussed here rely on the fact that all of the fields transform as simple tensors with no density weights. This is the case for the covariant formulation of BSSN and the standard gauge [17].

The cartoon BSSN code uses fourth-order Runge-Kutta for time integration. It uses standard fourth-order centered finite difference stencils for spatial derivatives, like those displayed in Eqs. (6). The only exceptions to this rule are the advection terms, which have the form  $\beta^a \partial_a F$  for a tensor or tensor component  $F$ . These terms are upwinded. The code as it is now written includes two layers of buffer points. This limits the size of the finite difference stencils such that the advection terms are only third-order accurate. For example, the finite difference approximation to  $\beta^z \partial_z F$  with  $\beta^z > 0$  is

$$(\beta^z \partial_z F)_k = \frac{1}{6h} \beta_k^z (-2F_{k-1} - 3F_k + 6F_{k+1} - F_{k+2}) \quad (\text{A7})$$

where  $k$  labels the grid points and  $h$  is the grid spacing. The overall accuracy of the cartoon code is limited to third order by the presence of these advection terms.

Figures 33 and 34 show the results of convergence tests for the cartoon code. The data for both of these figures come from a simulation in which a wormhole slice of Schwarzschild evolves into a trumpet geometry. The

data are taken at time  $t = 10$ . At this time the various fields, including the lapse function and shift vector, have settled fairly close to their trumpet values in the immediate vicinity of the puncture (say,  $r \lesssim 0.1$ ) but are still changing rapidly away from the puncture ( $r \gtrsim 0.1$ ).

Simulations at five different grid resolutions were used for these tests. Let us label these resolutions by integer subscripts 1, 2, 4, 8, and 16. The grid spacings are  $h_1 = 1/12.5$ ,  $h_2 = 1/25$ ,  $h_4 = 1/50$ ,  $h_8 = 1/100$ , and  $h_{16} = 1/200$ .

Figure 33 shows the absolute value of the Hamiltonian constraint. The curves in this figure are scaled by factors of 8 at successive resolutions, appropriate for a third-order numerical scheme. As one can see, the curves overlap in the limit of increasing resolution. This shows that the code is indeed third-order accurate.

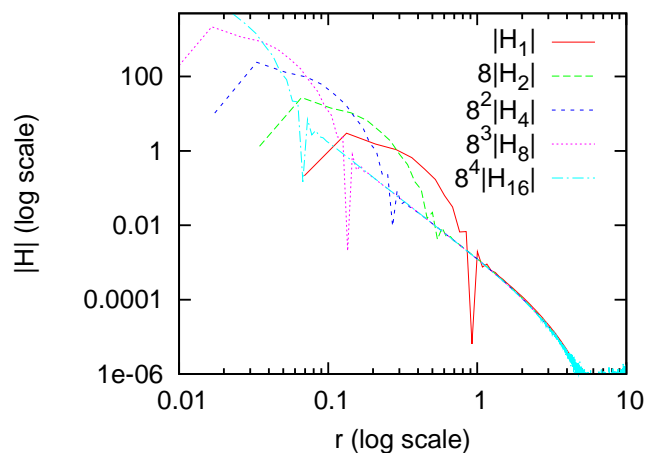


FIG. 33: Absolute value of the Hamiltonian constraint at five different resolutions. The curves are scaled by powers of 8 to show third-order convergence.

Figure 34 shows the result of a three-point convergence test for the conformal factor  $\varphi$ . Each curve is obtained from the difference between the conformal factor at successive resolutions, scaled by an appropriate power of 8. The curves in this plot also overlap in the limit of increasing resolution. This confirms that the code is third-order convergent.

These results require some elaboration. It has been stated in a number of publications that puncture evolution codes do not converge near the puncture. What we see from these figures is that the errors are large near the puncture. This does not imply a lack of convergence. A code is convergent if, at any given point in the computational domain, the scaled errors coincide with one another in the limit of high resolution. For example, consider the point  $r = 0.3$  on the graph of Fig. 33. This point is about half way between 0.1 and 1 on the logarithmic scale. The two lowest resolution curves do not coincide with the higher resolution curves at  $r = 0.3$ , due to the presence of large finite differencing errors. However, the

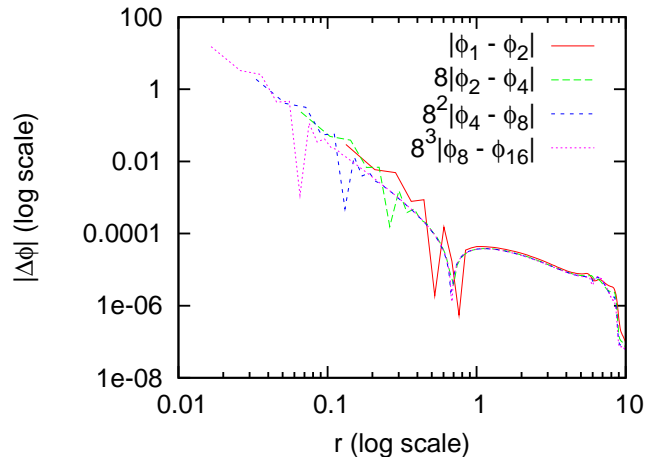


FIG. 34: Absolute value of the difference between the conformal factor at successive resolutions. The curves are scaled by powers of 8 to show third-order convergence.

three higher resolution curves overlap nicely. Thus, the code appears to be third-order convergent at  $r = 0.3$ .

Similarly, let us consider the point  $r = 0.1$ . None of the curves overlap at this point. This is due to insufficient resolution. It is fairly clear from examining the sequence of curves that if we were to add a higher resolution run, with  $h_{32} = 1/400$ , that the curves  $8^4|\mathcal{H}_{16}|$  and  $8^5|\mathcal{H}_{32}|$  would closely agree. We then expect that at  $r = 0.1$  the code is third-order convergent. In fact, the code appears to be third-order convergent at all points  $r > 0$ . This is as it should be since the data are smooth everywhere except at  $r = 0$ . A properly constructed code should be convergent at all points in the computational domain, excluding only the puncture points.

## APPENDIX B: TRUMPET GEOMETRY IN GAMMA-DRIVER COORDINATES

In Sec. V we considered the evolution of perturbations on a trumpet slice of a single Schwarzschild black hole. The perturbations were defined in terms of characteristic fields through Eqs. (25). This appendix is devoted to a description of the unperturbed trumpet geometry.

In this paper, the term “trumpet geometry” refers to a stationary 1+log slice of the Schwarzschild geometry. Such a slice can be expressed in various spatial coordinate systems. One technique for finding a trumpet slice in isotropic coordinates has been described elsewhere [10, 24]. What is needed for the analysis in Sec. V is a trumpet slice in stationary gamma-driver coordinates. That is, the data should satisfy the gamma-driver shift equations (10g,h) including advection terms and with

time derivatives set to zero:

$$0 = \beta^c \dot{D}_c \beta^a + \frac{3}{4} B^a, \quad (\text{B1a})$$

$$0 = \beta^c \dot{D}_c B^a - \beta^c \dot{D}_c \Lambda^a. \quad (\text{B1b})$$

The damping parameter  $\eta$  was set to zero in all simulations presented in this paper; it is set to zero here as well.

Let me begin by reviewing the construction of trumpet data in isotropic coordinates, then show how the results can be extended to stationary gamma-driver coordinates. A stationary, spherically symmetric geometry can be described by the metric

$$ds^2 = -(\alpha^2 + \beta^2)dt^2 + 2\beta d\ell dt + d\ell^2 + R^2 d\Omega^2 \quad (\text{B2})$$

where the lapse  $\alpha$ , shift  $\beta$ , and areal radius  $R$  are functions of the proper distance coordinate  $\ell$ . Recall that  $d\Omega^2 \equiv d\theta^2 + \sin^2\theta d\phi^2$  is the line element for the unit sphere. The Einstein equations imply

$$\alpha = R', \quad \alpha^2 - \beta^2 = 1 - 2M/R, \quad (\text{B3})$$

where  $M$  is an integration constant and the prime denotes  $\partial/\partial\ell$ . The 1+log slicing condition (10f), along with stationarity, gives

$$\alpha' = \frac{2\beta'}{\beta} + \frac{4R'}{R}. \quad (\text{B4})$$

Equations (B3) can be used to eliminate  $\alpha$  and  $\beta$  from Eq. (B4); this yields

$$R'' = \frac{2R'[3M - 2R + 2RR'^2]}{R[2M - R - 2RR' + RR'^2]}. \quad (\text{B5})$$

In Ref. [9], Hannam *et al.* argue that the numerator and denominator on the right-hand side of Eq. (B5) must vanish separately at some particular value of  $\ell$ . Solving these conditions simultaneously shows that the equations  $R' = -3 + \sqrt{10}$  and  $M/R = 4(-3 + \sqrt{10})$  must hold for some value of  $\ell$ .

Equation (B4) can be integrated to  $\beta R^2 = \sqrt{C}e^{\alpha/2}$ , where  $C$  is an integration constant. By using Eqs. (B3) we can rewrite this expression in terms of  $R$  and  $R'$ :

$$Ce^{R'} = R^4[R'^2 - 1 + 2M/R]. \quad (\text{B6})$$

The values previously obtained for  $R$  and  $R'$  at one value of  $\ell$  can be used to solve for the constant, with the result

$$C = \frac{M^4 e^{3-\sqrt{10}}}{128(\sqrt{10}-3)^3} \approx 1.55 M^4. \quad (\text{B7})$$

Note that in the limit as  $\ell \rightarrow -\infty$ , the trumpet geometry satisfies  $R' \rightarrow 0$ . Equation (B6) has two real solutions for  $R$  in this limit, but only one has  $R'$  approaching 0 through positive values. For that solution we find that the trumpet throat has radius  $R \approx 1.312 M$  in the limit  $\ell \rightarrow -\infty$ .

The proper distance can be written as

$$\ell = \int \frac{dR}{R'}, \quad (\text{B8})$$

where  $R'$  is considered to be a function of  $R$ . This dependence,  $R'$  as a function of  $R$ , is found by applying Newton's method to Eq. (B6). Then the integral (B8) can be evaluated numerically, starting from large negative  $\ell$  where  $R \approx 1.312 M$ . This gives  $\ell$  as a function of  $R$ .

Equivalently, the analysis above defines  $R$  as a function of  $\ell$ . The data  $\alpha$  and  $\beta$ , as functions of  $\ell$ , are found from Eqs. (B3). The components of the extrinsic curvature are computed from the spacetime metric (B2) as

$$K_{\ell\ell} = \beta \left( \frac{R''}{2R'} - \frac{2}{R} \right), \quad (\text{B9a})$$

$$K_{\theta\theta} = \beta R, \quad K_{\phi\phi} = \beta R \sin^2\theta. \quad (\text{B9b})$$

These are determined as functions of proper distance  $\ell$  from the numerical solution  $R(\ell)$ .

We now switch to isotropic coordinates, with spatial metric

$$ds^2 = \Psi^4(d\rho^2 + \rho^2 d\Omega^2). \quad (\text{B10})$$

Comparing with the spatial part of the metric (B2), we have  $\Psi = \sqrt{R/\rho}$  and  $\partial\rho/\partial\ell = \rho/R$ . Since  $R$  is known as a function of  $\ell$ , this second relation can be integrated numerically to give  $\rho$  as a function of  $\ell$ . Turning this around, we can consider  $\ell$  as a function of  $\rho$ . Then the conformal factor  $\Psi$  is determined as a function of the isotropic coordinate  $\rho$ : explicitly,  $\Psi = \sqrt{R(\ell(\rho))/\rho}$ . Likewise, the lapse function becomes a known function of the isotropic radius:  $\alpha = \alpha(\ell(\rho))$ . The shift vector in isotropic coordinates is  $\beta^\rho = (\rho/R)\beta$ , and the radial-radial component of the extrinsic curvature is  $K_{\rho\rho} = (R/\rho)^2 K_{\ell\ell}$ . These are now determined as functions of  $\rho$  since the dependence  $\ell(\rho)$  is known.

The stationary gamma-driver shift equations with  $\eta = 0$  are written in Eqs. (B1) above. Assuming  $\beta^a \neq 0$ , the second of these equations can be integrated to obtain  $B^a = \Lambda^a + \text{const}$ . We can choose initial data such that  $B^a = \Lambda^a$ . Then the first of Eqs. (B1) and the definition (9) for  $\Lambda^a$  yield

$$0 = g^{bc} \left( \Gamma_{bc}^a - \dot{\Gamma}_{bc}^a \right) + \frac{4}{3} \beta^c \dot{D}_c \beta^a. \quad (\text{B11})$$

Our goal is to find a change of spatial coordinates, from isotropic coordinates  $\rho, \theta, \phi$  to ‘‘gamma-driver coordinates’’  $r, \theta, \phi$ , such that Eq. (B11) is satisfied in the new coordinate system.

We begin by rewriting the spatial metric (B10) as

$$ds^2 = \Psi^4 \left( \frac{\rho^2 \rho'}{r^2} \right)^{2/3} \left[ \left( \frac{r \rho'}{\rho} \right)^{4/3} dr^2 + \left( \frac{r^2 \rho}{\rho'} \right)^{2/3} d\Omega^2 \right]. \quad (\text{B12})$$

Here,  $\rho'$  is the derivative of  $\rho$  with respect to the new radial coordinate  $r$ . Observe that the conformal part of this metric (the factor in square brackets) has determinant  $r^4 \sin^2 \theta$ . With this choice the conformal metric will have determinant 1 in Cartesian coordinates. Now use the conformal metric from Eq. (B12) to write the gamma-driver shift equation (B11) explicitly:

$$0 = \frac{1}{3r} \left( \frac{r\rho'}{\rho} \right)^{2/3} \left[ 6 - \frac{4\rho}{r\rho'} - \frac{2\rho^2}{r^2\rho'^2} + \frac{4\rho^2\rho''}{r\rho'^3} \right] + \frac{4}{3}\beta^\rho \left[ \frac{\beta^{\rho'}}{\rho'} - \frac{\beta^\rho\rho''}{\rho'^3} \right]. \quad (\text{B13})$$

$$r'' = \left[ (\rho r')^{7/3} + 2(\rho r')^{4/3}r - 3(\rho r')^{1/3}r^2 - 2\rho\beta^\rho\beta^{\rho'}r'^2r^{7/3} \right] \left[ 2\rho\beta^{\rho^2}r'^{7/3} - 2(\rho^2r')^{1/3}r \right]^{-1}. \quad (\text{B14})$$

It is helpful to make the change of variables  $\sigma \equiv r/\rho$ . The resulting equation can be solved for  $\sigma$  as a function of  $\rho$  with boundary conditions  $\sigma = 1$  as  $\rho \rightarrow 0$  and  $\rho \rightarrow \infty$ . Any number of techniques can be used; I use a simple multigrid relaxation scheme. Once we have found  $r$  as a function of  $\rho$ , the usual tensor transformation equations can be used to determine the lapse function, shift vector, and extrinsic curvature in the new coordinates  $r$ ,  $\theta$ , and  $\phi$ .

I have written a stand-alone numerical code to carry out the above calculations. Figure 35 is a plot of  $\sigma$  versus  $\rho$ . It is immediately clear that  $\sigma$  remains close to unity. Consequently the stationary gamma-driver coordinate  $r$  differs by a relatively small amount from the isotropic radius  $\rho$ .

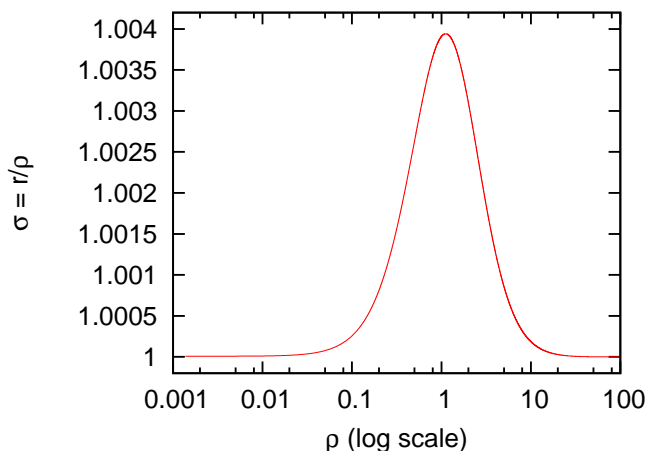


FIG. 35: The ratio  $\sigma = r/\rho$ , where  $r$  is the radial coordinate for the gamma-driver shift coordinates and  $\rho$  is the isotropic radius.

Figure 36 is a plot of the radial and angular compo-

Here, the shift has functional dependence  $\beta^\rho = \beta^\rho(\rho(r))$ .

Equation (B13) is a second order differential equation for  $\rho$  as a function of  $r$ . We can turn this around and view it as an equation for  $r$  as a function of  $\rho$ . In doing so, we must make the changes  $\rho' = 1/r'$  and  $\rho'' = -r''/\rho'^3$ , where primes on  $r$  denote derivatives with respect to  $\rho$ . With this view of Eq. (B13), the shift has functional dependence  $\beta^\rho = \beta^\rho(\rho)$ . Recall that  $\beta^\rho$  is known as a function of  $\rho$  from the numerical trumpet solution in isotropic coordinates.

The analysis above yields the following second order elliptic differential equation for  $r$  as a function of  $\rho$ :

nents of the conformal metric in the stationary gamma-driver coordinates. It is difficult to tell from this figure, but both components have a vanishing slope at  $r = 0$ . Figure 37 is a plot of the lapse function and Fig. 38 shows the radial components of the shift vector and the auxiliary field.

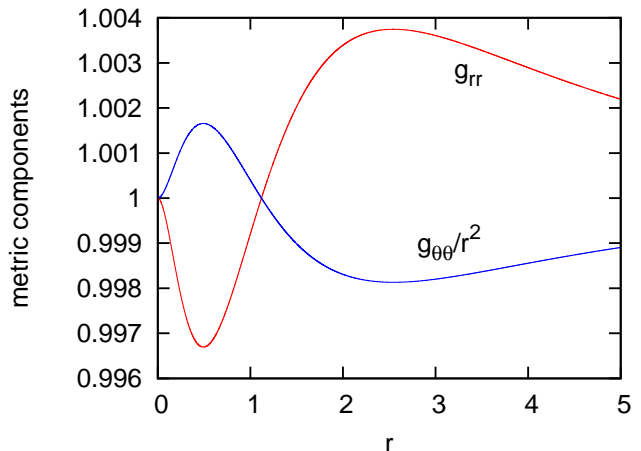


FIG. 36: Conformal metric components  $g_{rr}$  and  $g_{\theta\theta}/r^2$  for the trumpet geometry in gamma-driver shift coordinates.

The coordinate location of the black hole horizon in stationary gamma-driver shift coordinates is  $r = 0.842$ . (Again, as in the body of this paper, I have set  $M = 1$ .) In isotropic coordinates, the horizon location is  $\rho = 0.839$ . The location where  $e^{4\varphi} = 2\alpha$  and hyperbolicity breaks down is  $r = 4.06$  in stationary gamma-driver coordinates. To three significant digits, this location has the same value in isotropic coordinates:  $\rho = 4.06$ .

My original strategy for this research project was to use the stand-alone code to generate a very high resolution

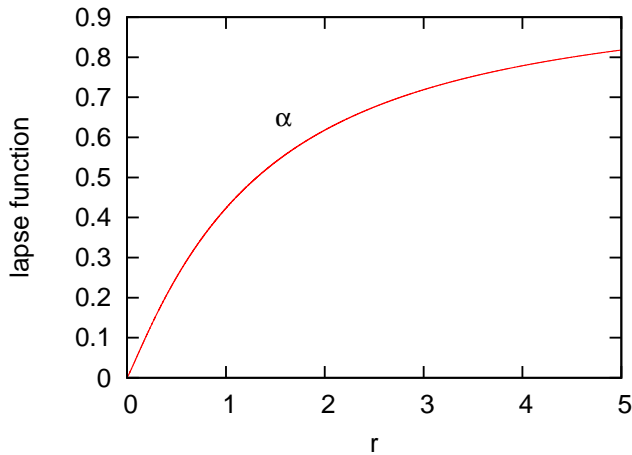


FIG. 37: Lapse function  $\alpha$  for the trumpet geometry in gamma-driver shift coordinates.

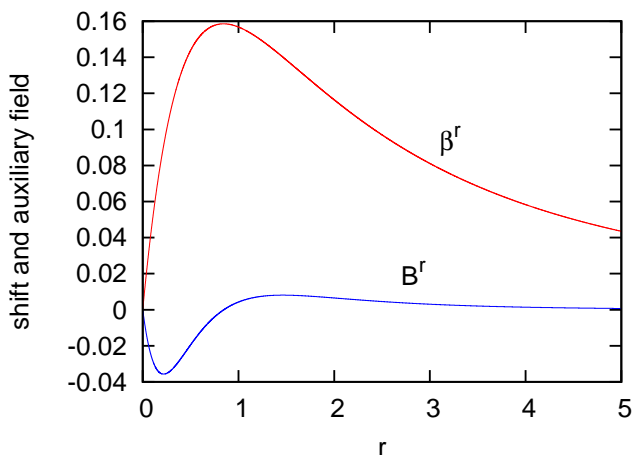


FIG. 38: Shift vector and auxiliary field components  $\beta^r$  and  $B^r$  for the trumpet geometry in gamma-driver shift coordinates.

data set for the unperturbed trumpet. That data would then be read into the cartoon BSSN code and interpolated onto the grid used for evolution. This strategy does not work very well. One of the difficulties is that there are many places in which numerical errors can accumulate. In particular, we have the integration in Eq. (B8), the integration of  $\partial\rho/\partial\ell = \rho/R$ , the solution of the elliptic Eq. (B14), the transformations from isotropic to stationary gamma-driver coordinates, and finally the interpolations onto the evolution grid. With my particular implementation, the errors in the unperturbed trumpet data were large enough to keep the evolution code from showing clean third-order convergence.

Another way that one can generate a trumpet geometry in gamma-driver coordinates is to begin with wormhole data and evolve that data until it settles to a stationary state. When a wormhole evolves to a trumpet,

there is an adjustment pulse that propagates out from the puncture boundary to infinity. It takes a time of about  $t = 100$  for the trailing edge of this pulse to propagate beyond  $r = 50$ . To be sure that the data are not contaminated with errors from the outer boundary, I evolve the initial wormhole for a time of  $t = 110$  on a grid with an outer boundary at  $r_{max} = 170$ . The data beyond  $r = 50$  is then discarded.

The unperturbed data produced by this second method, evolving a wormhole for  $t = 110$ , works fairly well for studies with initial perturbations in modes  $\chi_4^-$ ,  $\chi_5^-$ , and  $\chi_6^-$ . In these cases, with  $r_0 = 10$ , the perturbations reach the puncture boundary within a time of  $t \approx 20$  or less. A total simulation time of around  $t = 25$  is sufficient to reveal any reflections that might arise in mode  $\chi_6^+$ . With the outer boundary at  $r_{max} = 50$ , we can be confident that the results are not contaminated with errors from the outer boundary.

The studies with initial perturbations in  $\chi_1$ ,  $\chi_2$ , and  $\chi_3$  require much longer run times, up to  $t = 120$ . This is because these modes move very slowly toward the puncture. For these cases, the second method of generating unperturbed trumpet data would require us to evolve the wormhole for  $t \approx 180$  on a grid that extends to  $r_{max} \approx 300$ . This is not feasible with my current code. Thus, in Sec. V.D I used the first method, the method of Eqs. (B1) through (B14), to generate unperturbed trumpet data.

The two methods of calculating unperturbed trumpet data yield similar results. In fact, one cannot tell the difference between the two methods by examining graphs such as those in Figs. 36–38. The differences only appear upon more careful examination, such as convergence testing.

Another problem with the first method is that, near the puncture, the data is in some sense “too good”. For much of my work I used the first method to generate trumpet data with a resolution of  $\Delta r \approx 0.00069$ . That data was interpolated onto an evolution grid with a typical resolution of around  $h = 0.01$ . With the cartoon evolution code, as with any puncture method code, the resolution is very poor near the puncture boundary and the truncation errors are high. On the other hand, the truncation errors in the data produced by the first method are relatively low near the puncture boundary. Because of this mismatch, the unperturbed trumpet data is not quite stationary when it is evolved with the evolution code. In particular, the grid points near the puncture boundary evolve as they adjust to the larger truncation errors of the evolution code. This adjustment creates a perturbation that propagates outward through the computational domain. The adjustment is difficult to notice on a plot of the BSSN or gauge variables. However, the adjustment readily appears as an excitation in the characteristic fields near the puncture. In some cases the excitation is much larger than the perturbations we wish to study.

I can correct for this problem in the following way. For

each of the simulations with initial perturbations in  $\chi_1$ ,  $\chi_2$  and  $\chi_3$ , I “normalize” the data by subtracting the results obtained from a simulation with no perturbation. This removes the adjustment pulse from the data. The normalized data is easier to interpret than the raw data.

The same normalization scheme is applied to the simulations with initial perturbations in  $\chi_4^-$ ,  $\chi_5^-$  and  $\chi_6^-$ , but for a somewhat different reason. In these cases the unperturbed trumpet data is derived using the second method, the method of evolving a wormhole for  $t = 110$ . However, the mode analysis is very sensitive to any change in the stationary trumpet data. What can be seen in the mode plots is that the unperturbed trumpet data is not entirely stationary. Even after a run time of  $t = 110$  there is still a small amount of evolution taking place near the puncture boundary. For example, when the unperturbed trumpet data (prepared by the second method) is evolved for another  $t = 20$ , the value of mode  $\chi_6^+$  drifts from 0 to  $-2.5 \times 10^{-5}$  near the puncture boundary. These effects are removed from the data for perturbed trumpet

simulations by subtracting the data for an unperturbed trumpet simulation.

To summarize, the simulations from Sec. V that have initial perturbations in modes  $\chi_4^-$ ,  $\chi_5^-$  and  $\chi_6^-$  use the second method for generating unperturbed trumpet data. The simulations that have initial perturbations in modes  $\chi_1$ ,  $\chi_2$  and  $\chi_3$  use the first method for generating unperturbed trumpet data. In all cases, the data shown in Sec. V have been normalized by subtracting the data obtained from a simulation of the unperturbed trumpet.

## ACKNOWLEDGMENTS

I would like to thank Bernard Kelly, Richard Price, Manuel Tiglio and James van Meter for helpful comments. This work was supported by NSF Grant No. PHY-0758116.

- 
- [1] M. Campanelli, C. O. Lousto, P. Marronetti, and Y. Zlochower, *Phys. Rev. Lett.* **96**, 111101 (2006), gr-qc/0511048.
  - [2] J. G. Baker, J. Centrella, D.-I. Choi, M. Koppitz, and J. van Meter, *Phys. Rev. Lett.* **96**, 111102 (2006), gr-qc/0511103.
  - [3] M. Shibata and T. Nakamura, *Phys. Rev.* **D52**, 5428 (1995).
  - [4] T. W. Baumgarte and S. L. Shapiro, *Phys. Rev.* **D59**, 024007 (1998), gr-qc/9810065.
  - [5] C. Bona, J. Masso, E. Seidel, and J. Stela, *Phys. Rev. Lett.* **75**, 600 (1995), gr-qc/9412071.
  - [6] M. Alcubierre, B. Brüggmann, P. Diener, M. Koppitz, D. Pollney, E. Seidel, and R. Takahashi, *Phys. Rev.* **D67**, 084023 (2003), gr-qc/0206072.
  - [7] J. D. Brown, *Phys. Rev.* **D77**, 044018 (2008), 0705.1359.
  - [8] J. D. Brown, *Class. Quant. Grav.* **25**, 205004 (2008), 0705.3845.
  - [9] M. Hannam, S. Husa, D. Pollney, B. Bruegmann, and N. O’Murchadha, *Phys. Rev. Lett.* **99**, 241102 (2007), gr-qc/0606099.
  - [10] M. Hannam, S. Husa, F. Ohme, B. Bruegmann, and N. O’Murchadha, *Phys. Rev.* **D78**, 064020 (2008), 0804.0628.
  - [11] Z. B. Etienne, J. A. Faber, Y. T. Liu, S. L. Shapiro, and T. W. Baumgarte, *Phys. Rev.* **D76**, 101503 (2007), 0707.2083.
  - [12] J. D. Brown, O. Sarbach, E. Schnetter, M. Tiglio, P. Diener, I. Hawke, and D. Pollney, *Phys. Rev.* **D76**, 081503 (2007), 0707.3101.
  - [13] J. D. Brown, P. Diener, O. Sarbach, E. Schnetter, and M. Tiglio, *Phys. Rev.* **D79**, 044023 (2009), 0809.3533.
  - [14] O. Sarbach, *J. Phys. Conf. Ser.* **91**, 012005 (2007), 0708.4266.
  - [15] H. R. Beyer and O. Sarbach, *Phys. Rev.* **D70**, 104004 (2004), gr-qc/0406003.
  - [16] C. Gundlach and J. M. Martin-Garcia, *Phys. Rev.* **D74**, 024016 (2006), gr-qc/0604035.
  - [17] J. D. Brown, *Phys. Rev.* **D79**, 104029 (2009), 0902.3652.
  - [18] M. Alcubierre, S. Brandt, B. Bruegmann, D. Holz, E. Seidel, R. Takahashi, and J. Thornburg, *Int. J. Mod. Phys.* **D10**, 273 (2001), gr-qc/9908012.
  - [19] J. D. Brown, *Phys. Rev.* **D71**, 104011 (2005), gr-qc/0501092.
  - [20] D. Garfinkle, C. Gundlach, and D. Hilditch, *Class. Quant. Grav.* **25**, 075007 (2008), 0707.0726.
  - [21] J. R. van Meter, J. G. Baker, M. Koppitz, and D.-I. Choi, *Phys. Rev.* **D73**, 124011 (2006), gr-qc/0605030.
  - [22] H. O. Kreiss and O. E. Ortiz, *Lect. Notes Phys.* **604**, 359 (2002), gr-qc/0106085.
  - [23] G. Nagy, O. E. Ortiz, and O. A. Reula, *Phys. Rev.* **D70**, 044012 (2004), gr-qc/0402123.
  - [24] B. Bruegmann, *Gen. Rel. Grav.* **41**, 2131 (2009), 0904.4418.